The Astrophysical Journal, 767:170 (18pp), 2013 April 20 doi:10.1088/0004-637X/767/2/170


# KELVIN–HELMHOLTZ INSTABILITY OF THE CME RECONNECTION OUTFLOW LAYER IN THE LOW CORONA

Claire Foullon[1], Erwin Verwichte[1], Katariina Nykyri[2], Markus J. Aschwanden[3], and Iain G. Hannah[4]
[1] Centre for Fusion, Space and Astrophysics, Department of Physics, University of Warwick, Coventry CV4 7AL, UK; claire.foullon@warwick.ac.uk
[2] Department of Physical Sciences, Embry-Riddle Aeronautical University, Daytona Beach, FL 32114, USA
[3] Lockheed Martin Solar and Astrophysics Laboratory, 3251 Hanover Street, Palo Alto, CA 94304, USA
[4] School of Physics & Astronomy, University of Glasgow, Glasgow G12 8QQ, UK
*Received 2012 August 3; accepted 2013 March 13; published 2013 April 8*

## ABSTRACT

New capabilities for studying the Sun allow us to image for the first time the magnetic Kelvin–Helmholtz (KH) instability developing at the surface of a fast coronal mass ejecta (CME) less than 150 Mm above the solar surface. We conduct a detailed observational investigation of this phenomenon, observed off the east solar limb on 2010 November 3, in the EUV with *SDO*/AIA. In conjunction with *STEREO-B*/EUVI, we derive the CME source surface position. We ascertain the timing and early evolution of the CME outflow leading to the instability onset. We perform image and spectral analysis, exploring the CME plasma structuring and its parabolic flow pattern. As we evaluate and validate the consistency of the observations with theoretical considerations and predictions, we take the view that the ejecta layer corresponds to a reconnection outflow layer surrounding the erupting flux rope, accounting for the timing, high temperature (∼11.6 MK), and high flow shear (∼680 km s$^{-1}$) on the unstable CME northern flank and for the observed asymmetry between the CME flanks. From the irregular evolution of the CME flow pattern, we infer a shear gradient consistent with expected spatial flow variations across the KH-unstable flank. The KH phenomenon observed is tied to the first stage of a linked flare–CME event.

*Key words:* instabilities – plasmas – solar-terrestrial relations – Sun: corona – Sun: coronal mass ejections (CMEs) – Sun: oscillations

*Online-only material:* color figures

## 1. INTRODUCTION

Coronal mass ejections (CMEs) are primarily detected through white light observations by coronagraphs. Most of the associated observations in the lower corona at heights below 1–2 $R_\odot$ (e.g., solar flares, erupting prominences, disappearing filaments, post-eruptive arcades, coronal dimming) do not indicate the exact structure of the CME and are phenomena associated by either a common cause, or by a secondary reaction to the CME launch itself (e.g., Howard 2011). Hence, while the inner corona observations can give an indication of the source region of a CME, the correspondence with coronagraph CMEs is not immediate. From both general theoretical and observational points of view, the main structural components of a fast CME include a flux rope (e.g., Chen et al. 1997, and references therein) contained within an overlying ejecta, preceded by a sheath and a shock (e.g., Illing & Hundhausen 1985; Steinolfson & Hundhausen 1990; Liu et al. 2009, and references therein). On its way to outer coronal heights, a CME flux rope may develop via magnetic reconnection, with the transformation of an initial arcade or with new flux surfaces and mass added to the flux rope (Chen & Kunkel 2010, and references therein). In the solar wind, at much larger distances from the Sun (>50 $R_\odot$), an interplanetary coronal mass ejection (ICME) is regarded as the heliospheric counterpart of the CME with comparable structural components (e.g., Burlaga et al. 1981; Arge et al. 2004; Foullon et al. 2007; Siscoe & Odstrcil 2008; Das et al. 2011, and references therein), while further transformations attributed to reconnection processes are observed (e.g., Farrugia et al. 2001; Ruffenach et al. 2012).

For the first time, Foullon et al. (2011, hereafter F11), imaged the magnetic Kelvin-Helmholtz (KH) instability, developing at the surface of a fast CME less than 150 Mm above the solar surface in the inner corona. This was rendered possible with the Atmospheric Imaging Assembly (AIA; Lemen et al. 2012) on board the *Solar Dynamics Observatory* (*SDO*). The phenomenon appears in the magnetized corona, on the flank of a CME that clearly shows magnetic flux rope like properties (see Figure 3(a) of F11 and also Cheng et al. 2011; Savage et al. 2012, for extensive theoretical and observational supportive background to this interpretation). Thus, modeling the phenomenon inherently requires inclusion of the magnetic field or at least consideration of the extent to which the magnetic field plays a role. To our knowledge few numerical simulations of CMEs considered the occurrence of the KH instability, but none predicted the KH phenomenon in the magnetized corona. In their solar wind simulations, Manchester et al. (2005) find azimuthal flows of about 100 km s$^{-1}$ forming in the CME-sheath behind a bow shock: since their cavity is the flux rope, they suggest that such flows could be susceptible to KH instabilities. In the corona, Pagano et al. (2007) obtained the KH instability in hydrodynamic simulations but not in their magnetic field numerical experiments; aspects of simulations by Terradas et al. (2008) developed for moving magnetic flux tubes become relevant if related to cross-sections of CME flux ropes; finally Ofman & Thompson (2011, 2012) presented complementary simulations for on-disk observations, which differ in many aspects with our off-limb observations in the corona.

In the simplest linear magnetohydrodynamic (MHD) description, the onset condition for the KH instability in an ideal incompressible plasma, with a discontinuous velocity shear layer and assuming the layer to be infinitely thin (i.e., in the limit of no boundary layer or long wavelengths; Chandrasekhar 1961; Talwar 1964; Hasegawa 1975), is

$$[\mathbf{k}\cdot(\mathbf{V_1}-\mathbf{V_2})]^2 > \frac{n_1+n_2}{\mu_0 m_p n_1 n_2}[(\mathbf{k}\cdot\mathbf{B_1})^2+(\mathbf{k}\cdot\mathbf{B_2})^2]. \quad (1)$$

Here the indices refer to the two plasma environments on either side of the boundary, $n$ is the plasma number density, $m_p$ the proton mass, $\mu_0$ the permeability of free space, $\mathbf{V}$ is the plasma flow velocity, $\mathbf{B}$ the magnetic field vector, and $\mathbf{k}$ the wave vector; $\mathbf{V}$, $\mathbf{B}$, and $\mathbf{k}$ are all tangential to the layer. The phase speed of the KH wave is

$$v_p = \frac{n_1 \mathbf{k}\cdot\mathbf{V_1} + n_2 \mathbf{k}\cdot\mathbf{V_2}}{k(n_1+n_2)}, \quad (2)$$

from which the group velocity, $\mathbf{v_g}$, ensues, i.e.,

$$\mathbf{v_g} = \frac{\partial\omega}{\partial\mathbf{k}} = \frac{n_1\mathbf{V_1} + n_2\mathbf{V_2}}{n_1+n_2}. \quad (3)$$

As Equation (1) shows, KH waves are caused by a velocity gradient or shear, $|\mathbf{V_1} - \mathbf{V_2}|$, between the streaming CME and relatively stagnant background coronal plasmas, in the case of the CME-pause. The instability criterion is more likely to be met for wave propagation in the direction of maximum sheared flow. Moreover, the threshold above which KH instability may occur (i.e., the right-hand side in Equation (1)) is reduced in the regions of low or high magnetic shear, between the ejecta and coronal field lines and for wave propagation perpendicular to the magnetic fields: this part corresponds to stabilizing effects from magnetic tension forces (e.g., Chandrasekhar 1961) that are weakened for ejecta and coronal magnetic field lines both perpendicular to the flow shear, i.e., both parallel to the solar surface.

The KH instability observational discovery at the Sun has major implications for our understanding of CME formation and dynamics. Many CME characteristics, plasma parameters, flow and magnetic field vector properties, can be inferred from KH instability phenomenon observational properties, whether the CME properties are initially acquired during the CME formation or evolved during its propagation. Several questions arise from the observational characteristics of the unstable ejecta, which occurred on 2010 November 3. To begin with, the instability is detected in the highest AIA temperature channel only, centered on the 131 Å EUV bandpass at 11 MK. In this temperature range, the ejecta lifting off from the solar surface forms a bubble of enhanced emission against the lower density ambient corona. Moreover, the observations show the KH waves occurring on the northern flank of the ejecta only. Finally, the phenomenon ceases to be observed rapidly. Several preliminary explanations and scenarios have been suggested, but there are no firm conclusions as yet.

Other complementary aspects of the same CME event have been presented by Reeves & Golub (2011), Cheng et al. (2011), Woods et al. (2011), White & Verwichte (2012), Bain et al. (2012), Savage et al. (2012), White et al. (2012), and Zimovets et al. (2012). In particular, Bain et al. (2012) showed that the associated shock, outlined by type II radio emission, propagates at $\sim$1960 km s$^{-1}$ up to 500 Mm in the low corona, much faster than the erupting CME, and concluded that for the case of a CME-driven shock this is consistent with the characteristics of a piston-driven shock, rather than a bow-shock wave. Accordingly, the CME structure acts like a spherical piston and expands in such a way that the ambient plasma is unable to flow behind the CME or driver. The question arises as to what then is causing the flow shear in the leading ejecta layer as indicated by the presence of the KH waves.

To answer these questions, we further investigate the phenomenon and the overall conditions leading to or resulting from the KH instability in the CME event reported. In the context of a theoretical two-dimensional (2D) description of the KH unstable surface, we also aim to derive the most realistic local input values defining the initial equilibrium states of the KH instability. In Section 2, we explore the CME dynamics and origins, deriving its 3D trajectory and the timing of the instability onset. In Section 3, we explore the multi-wavelength capabilities of AIA to derive plasma parameters and describe any plasma structuring accompanying the development of the KH waves. In Section 4, we quantify and discuss rates of shear resulting from the KH wave activity. In Section 5, we discuss the nature of the KH unstable interface (identifying the cause of the flow shear and determining the circumstances for the occurrence of linear KH instability in terms of magnetic field and velocity shear). Section 6 gives a summary of the results from this investigation.

## 2. CME DYNAMICS AND ORIGINS

### 2.1. 3D Trajectory from STEREO-B and Earth-view Images

On 2010 November 3, Solar TErrestrial RElations Observatory Behind (*STEREO-B*) is located eastward of *SDO* by 82° of heliolongitude, and may be used in conjunction with *SDO* to give some indication of the magnetic field topology and flow pattern. At the time of the event, Extreme Ultraviolet Imager (EUVI) from *STEREO*'s Sun–Earth Connection Coronal and Heliospheric Investigation (SECCHI) instrument suite (Howard et al. 2008) achieved the highest temporal resolution in the 195 Å bandpass: EUVI images of the active region on the disk are taken every 5 minutes in this bandpass. Figure 1 shows the *STEREO-B* view of the active region (pre-NOAA 11121) with the trace of the east solar limb as seen from *SDO* (white line, upper panels), which indicates that the associated flare and the eruption originate outside the *SDO* plane-of-the-sky (POS), from eastward or "behind" the east solar limb as seen from *SDO* (lower panels).

To assist with our comparison, we use field line reconstructions from a Potential Field Source Surface (PFSS) model (Schrijver & De Rosa 2003) providing an approximate description of the solar coronal magnetic field based on photospheric fields (*SOlar and Heliospheric Observatory* (*SOHO*)/Michelson Doppler Imager (MDI) magnetograms) observed over the past Carrington rotation. Combined with the EUV images, the reconstructed field lines are rough estimates, that do not model the magnetic field structure of the CME itself, but provide visual aids to deduce the 3D-geometry of the ejecta at the time and thus the main orientation of its magnetic field topology. The central axis of the flux rope is envisioned to be quasi-perpendicular to the *SDO* POS in those observations. The left panels of Figure 1 show PFSS closed loop shapes of a streamer that fit dimming in the *STEREO-B* EUVI 195 Å difference image and are overarching the emission contours of the *SDO* AIA 131 Å image. As pointed out by Cheng et al. (2011, see their Figure 4), the dimming region obtained by taking a difference image in AIA 193 Å corresponds to the hot emitting ejecta region in AIA 131 Å. AIA 193 Å and SECCHI/EUVI 195 Å are very similar bandpasses, showing EUV emission at 1.6 MK.

The EUV images and PFSS field lines are also shown in the context of the larger fields of view provided by coronagraphs in both vantage points (*SOHO*'s Large Angle and Spectroscopic Coronagraph (LASCO) C2 (Brueckner et al. 1995) and *STEREO-B*/SECCHI/COR1). All together these figures show the relative smaller size of the initial AIA 131 Å ejecta compared with the size of the helmet streamer and how the CME is guided apparently by the streamer toward the equator. Beforehand, the closed loops of the streamer core form a canopy of field lines

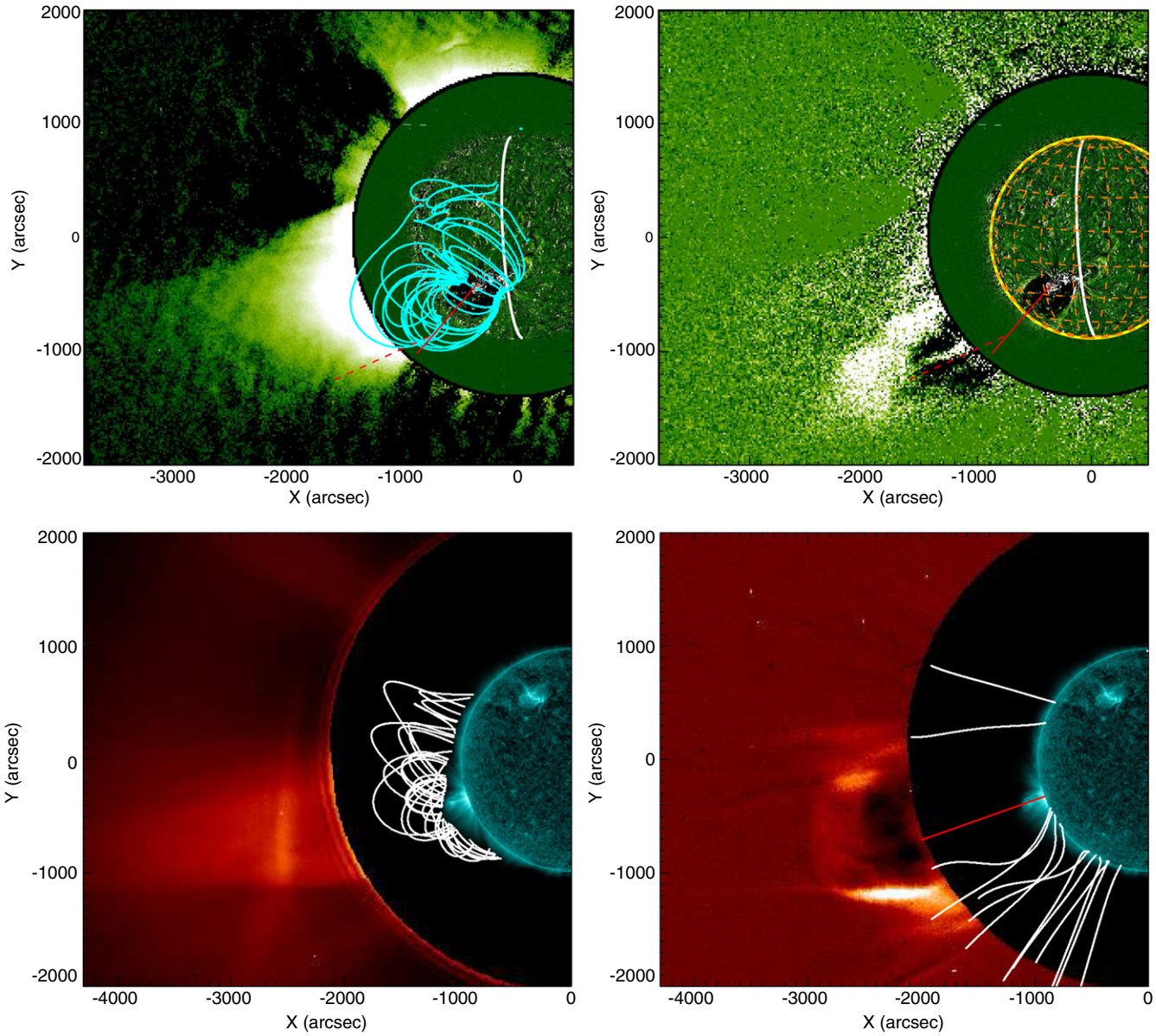


**Figure 1.** (Upper) *STEREO* and (lower) Earth views of the solar corona on 2010 November 3 combining coronagraph and EUV images. The red line is the projection in the POS of the inner CME axis of propagation, oriented radially outward from the heliographic source position (S20, E-14)°. Overlaid are (left) closed and (right) open PFSS field lines defined by a bounding box (90° latitude × 50° longitude wide, centered on the source latitude and extending behind from the *SDO* limb), outside of which no field line starting points (at 1.5 $R_{\odot}$) lie. (Upper) *STEREO-B*/SECCHI/COR1 coronagraph images (left is at 12:35:58 UT, right is the 13:56:16–13:16:16 UT difference image) and EUVI 195 Å (12:16:28–12:11:28 UT) difference image; overlaid are the *SDO* limb (white) and in the right panel, heliospheric grid lines spaced by 20° (orange dashed lines) and a deflection trace (red dashed line). (Lower) *SOHO*/LASCO/C2 coronagraph images (left is at 12:12:07 UT, right is the 12:48:06–12:36:06 UT difference image) and *SDO*/AIA 131 Å 12:15:34 UT image; in the left panel, the closed field lines are traced behind 131 Å coronal emission.
(A color version of this figure is available in the online journal.)

oriented primarily perpendicular to the ejecta flow, which finds its way through. The coronagraph observations confirm that the ejecta trajectory starts near the flare site, on the streamer surface axis, and points upward through the streamer against the direction of gravity. This trajectory direction is thus given by the heliographic coordinates of the ejecta source: $20^{\circ} \pm 0.^{\circ}1$ south and $-14^{\circ} \pm 0.^{\circ}5$ in longitude behind the east limb. A projection factor, $f = 1/\cos 14^{\circ} = 1.03$, is needed to correct distances measured in the *SDO* plane of sky, back to this trajectory.

### 2.2. Timing of CME Outflow Source

The associated (occulted) C4.9 class flare observed by the *Geostationary Operational Environmental Satellite* (*GOES*) is recorded to start at 12:07 UT, peak at 12:21 UT and end at 12:33 UT. In the 12–25 keV energy range of *RHESSI*, this corresponds to two flares, and the start of the rising phase in the *GOES* flare coincides with the start at 12:11:44 UT of the second flare in *RHESSI* (peaking at 12:17:14 UT, see *RHESSI* flare list[5]). Based on coronagraph observations, CME evolution has been found to follow three distinct phases: *initiation* phase, *acceleration* phase, and *propagation* phase, which correspond respectively to the pre-flare phase, rise phase, and decay phase of the associated soft X-ray flaring emission (Zhang & Dere 2006). During the initiation phase (12:07–12:11:44 UT: *GOES* pre-flare or first *RHESSI* flare), it is assumed that the flux rope is formed and is slowly rising.

[5] http://hesperia.gsfc.nasa.gov/rhessidatacenter/

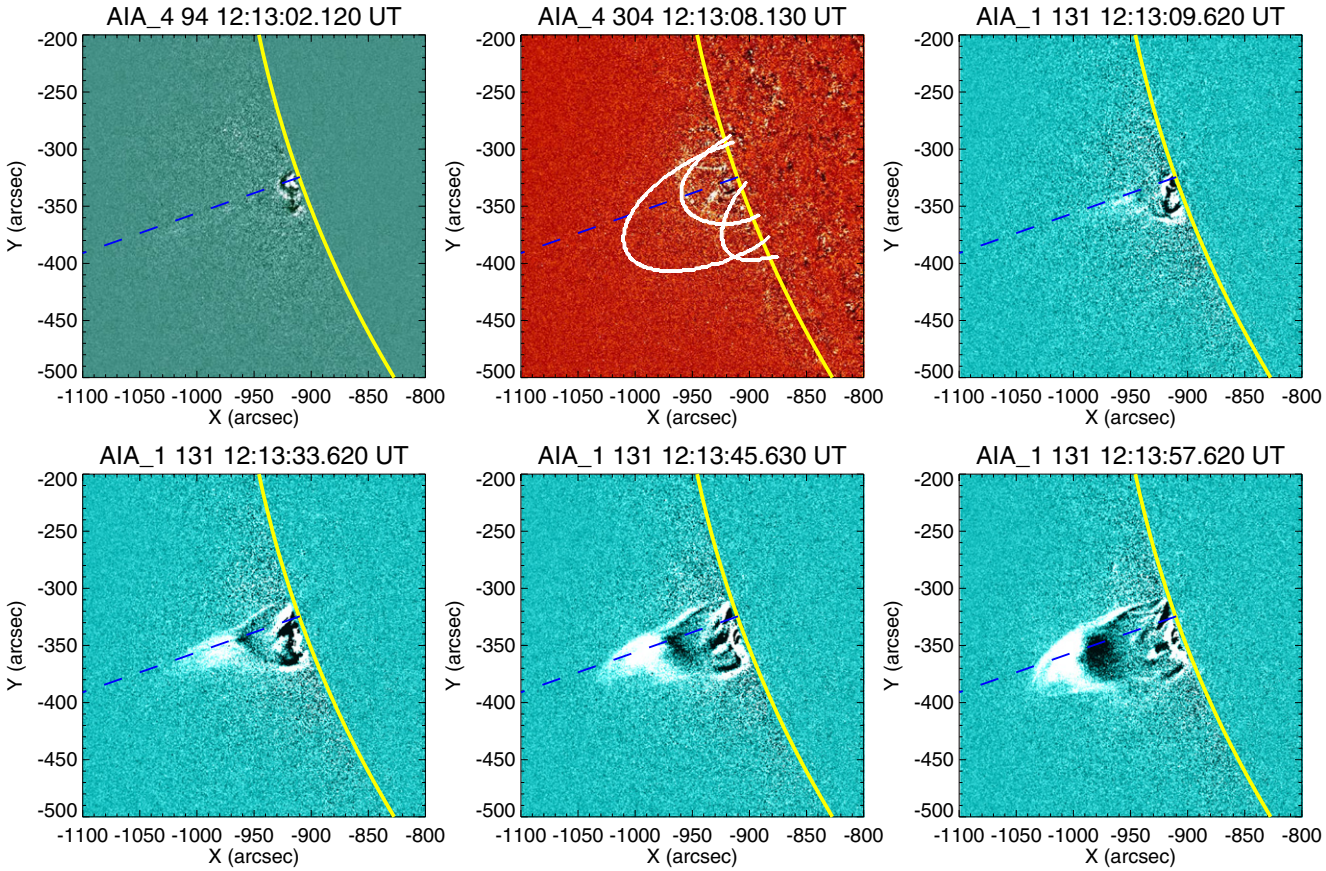


**Figure 2.** *SDO*/AIA time running difference images of the southeast solar limb on 2010 November 3 (with time indicated of the latest image). Upper: first indications in 94, 304, and 131 Å images of an outflow acceleration jet ($t_0$ = 12:13:00 UT ±2 s); lower: 131 Å sequence showing the ejecta layer or acceleration jet (entrained with an embedded brighter core, attributed to a flux rope), filling out with hot plasma the space below a canopy of overlying field lines and providing a possible return flow on the southern flank. The thin dashed blue line is the projection in the POS of the axis of propagation, oriented radially outward from the heliographic source position (S20, E-14)°. In the 304 Å image, the overlaid PFSS field lines (in white) are defined by a bounding box, 4 × 4° wide and centered on this source position, outside of which no field line starting points (at 1.05 $R_\odot$) lie.

(A color version of this figure is available in the online journal.)

What is of relevance here is the onset time of the accelerated plasma surrounding the flux rope. In the high-speed lower coronal event studied, it is reasonable to assume that the time of initial conditions for the *instability* onset, $t_0$, happens within the CME acceleration phase, when the instability threshold in velocity (and shear) is reached. Our purpose is to obtain an estimate of the lag time $\Delta t$, with respect to this initial time, for the appearance of the first perturbations on the ejecta surface that then lead to the well-formed KH waves. $t_0$ is expected after the soft X-ray rising onset (12:11:44 UT), which generally coincides with the coronagraph CME acceleration onset.

In Figure 2, the sequence of AIA images shows evidence for the jet origin of the CME, most recognizable in its elongated structure above a bipolar arcade at 12:13:33 UT. As shown in the lower panels, the outflow jet layer (entrained with an embedded brighter core, attributed to a flux rope) is subsequently entrapped by overlying fields, providing a possible return flow on the southern flank.

As shown in the upper panels, the first outflow jet appears not earlier than 12:13:09 UT in 131 Å AIA images, which places the timing of the outflow at 12:13:03 UT ±6 s; an earlier indication of the jet can be found at 12:13:02 UT in 94 Å and 12:13:08 UT in 304 Å AIA images, narrowing the timing of the outflow down to $t_0$ = 12:13:00 UT ±2 s. This timing is in agreement with the onset of the hard X-ray flare in *RHESSI* light curves at non-thermal energies above 25 keV, indicative of the first peak acceleration of the most energetic electrons and their possible thermalization, heating the plasma at lower energies (e.g., Foullon et al. 2010, for 10 MK coronal sources). Thus we obtain an estimate $\Delta t = 111 \pm 8$ s between the first high-temperature acceleration jet and the first perturbations observed on the ejecta surface (12:14:51 UT ±6 s).

## 3. AIA MULTI-WAVELENGTH ANALYSIS

The multi-wavelength information from AIA coronal temperature filters or bandpasses may be combined in a way to derive electron plasma parameters and to spatially identify the plasma structuring accompanying the development of the KH instability. Differential Emission Measure (DEM) techniques may be valid for application to the overall structure of the CME in quasi-static snapshots. The difficulty lies in separating foreground from background emission. In this respect, a sharp boundary or structuring may give some handle to the application of a DEM analysis and, in the following (Section 3.1), we first derive average plasma parameter values across the ejecta surface using two different methods (one for each side of the ejecta). However, the dynamic nature of the KH wave phenomenon (relatively fast) on smaller scales combined with the instrument delays of up to 6 s between wavelengths can undermine the applicability of this kind of analysis for mapping the parameters of relatively small and dynamic "non-static" structures. We then propose (Section 3.2) an alternative method, based on filter ratios of

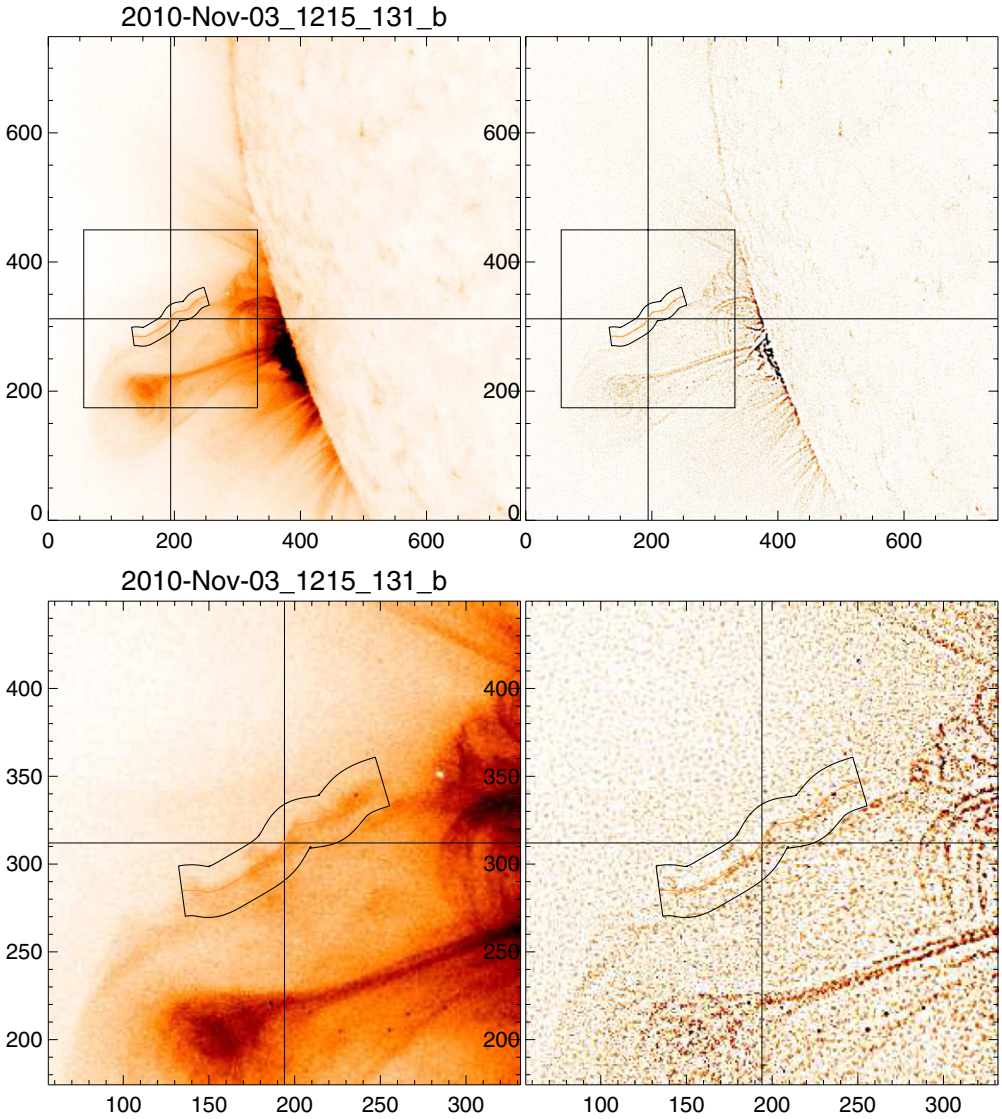


**Figure 3.** Left: 131 Å AIA image taken on 2010 November 3, at 12:15:21 UT; right: corresponding highpass-filtered image to enhance and trace the ejecta surface. The overlaid cross-haired square region in the upper panels is shown in the lower panels. The automated tracing of the ejecta surface allows one to define a segment with nine positions, $s$, along it, and oriented toward higher heights (from right to left in the image).

(A color version of this figure is available in the online journal.)

intensities above a time-averaged corona, to give a qualitative overview of the dynamic plasma structuring. The thinking is quite different and it would be beyond the scope of this paper to make comparisons between methods. Rather we are seeking meaningful results in each case to help us pursue our investigation.

### *3.1. DEM Spectral Analysis*

Using six AIA coronal bandpasses, we derive electron temperatures and densities on the northern flank of the ejecta where the instability takes place. We first select a segment formed of nine cross-sections along this undulating flank region, and centered on the ejecta layer as observed in 131 Å at 12:15:21 UT (see Figure 3). For each cross-section or position $s$ along the segment, we then apply a DEM spectral procedure; this procedure has been devised for one dimensional structures such as coronal loops, whose width in the line-of-sight (LOS) is assumed to be similar than the one measured in the POS (Aschwanden & Boerner 2011; Aschwanden et al. 2013). The method can be applied here on the edge of the ejecta, where the width of KH billows or the associated ejecta layer is expected to be similar to its LOS extent.

The procedure is illustrated in Figure 4. Similarly to the analysis of loop structures, a linear background flux profile $B_\lambda$ is obtained in the direction perpendicular to the segment for each position $s$ and wavelength $\lambda$. Note that this linear profile is inclined between background levels attributed to the main ejecta and the ambient corona, and whose difference is more pronounced in the case of the 131 Å image. A Gaussian cross-sectional profile is fitted in each case and the background-subtracted layer fluxes, $F_\lambda^{\rm mod}(s)$, are used for a double-Gaussian DEM forward fit with measurements of the temperatures, $T_e(s)$, temperature widths, $\sigma_T(s)$, electron densities, $n_e(s)$, and layer widths, $w(s)$. There is an indication that the temperature is decreasing outward along the layer segment. Averaging over the segment length, we obtain plasma parameter estimates for the ejecta layer of $T_e = 11.6 \pm 3.8$ MK and $n_e = (7.1 \pm 1.6) \times 10^8\,{\rm cm}^{-3}$, together with a layer width of $4.1 \pm 0.7$ Mm.

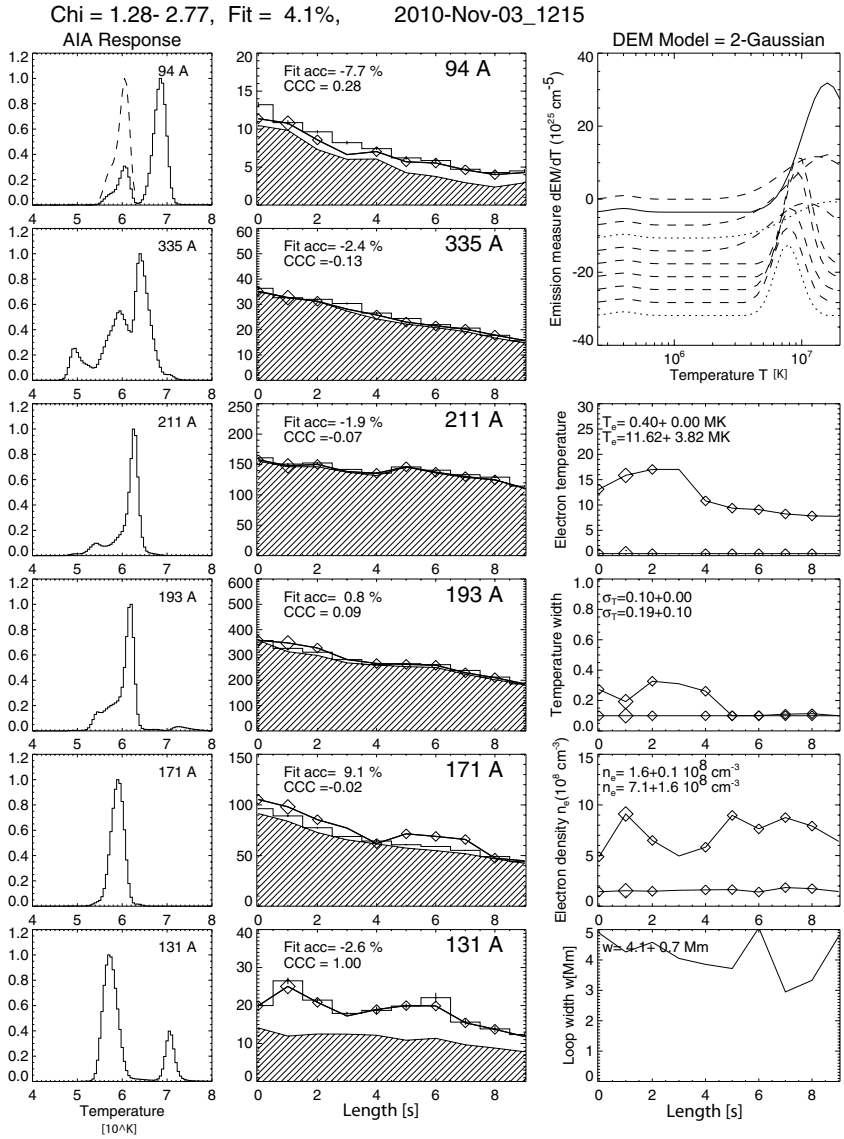


**Figure 4.** Left column: sequence of temperature responses from six AIA bandpasses with an empirical correction for the 94 Å response function (dashed line; see Aschwanden & Boerner 2011). Middle column: corresponding integrated flux profiles along the CME segment with background fluxes $B_\lambda(s)$ (hatched), total fluxes $F_\lambda(s)$ (solid curve with error bars), and best fits $F_\lambda^{\rm mod}(s)$ with the double-Gaussian DEM; the fit accuracy (in percent) is indicated in each panel. Right column: sequence showing in the vertical direction: double-Gaussian DEM fits, best-fit values along the segment of the DEM peak temperatures ($T_e(s)$), Gaussian temperature widths ($\sigma_T(s)$) (error bars in temperature), electron densities ($n_e(s)$), and layer widths ($w(s)$).

In a quiet corona, we expect $T_e \sim 1$ MK. Density estimates (Aschwanden & Acton 2001) vary from (2 to 1) $\times 10^8$ cm$^{-3}$ between 0.05 and 0.15 $R_\odot$ (40–100 Mm), at heights where we start to see the KH waves developing. In the above DEM analysis, we would require some LOS convolution model to provide plasma parameter estimates for the ambient corona. Instead, we apply a regularized inversion method to the AIA multi-wavelength data set, designed to recover DEMs from multi-wavelength observations (Hannah & Kontar 2012, 2013). We obtain spatial Emission Measure maps of $n_e^2 h$ values, where $h$ is the length of LOS integration, for different temperature bins. Figure 5 presents such maps obtained around 12:15:02 UT, for 2–4 MK and 4–6 MK. Both maps show a "CME-sheath" in the leading edge and northern flank, with values of $5 \times 10^{27}$ cm$^{-5} \leqslant n_e^2 h \leqslant 10^{28}$ cm$^{-5}$. Assuming an axially symmetric CME and taking account of the small trajectory angle out of the POS, we infer a minimum length of LOS integration, $h = 80$–$84$ Mm, for the lowest DEM values at the CME leading edge. It is expected that the CME extends longitudinally up to the width of the arcade, as shown in the difference *STEREO-B* EUVI image (Figure 1), and we associate a maximum $h = 250$ Mm with the highest DEM value on the northern flank. With these extrema, we obtain $n_e = (7.1 \pm 0.8) \times 10^8$ cm$^{-3}$ and, surprisingly, recover the average density value in the ejecta layer.

### 3.2. Filter Ratio Region Maps

In order to map relatively small and dynamic structures, average background subtraction and alignment to a common spatial and temporal frame are necessary prior to combining the multi-wavelength information. The image treatment is done on snapshots of the region of interest (ROI) presented in F11. The images are taken every 12 s, but not simultaneously in every bandpass. Figure 6 is an example of a composite time–distance image, obtained after treatment, using data from

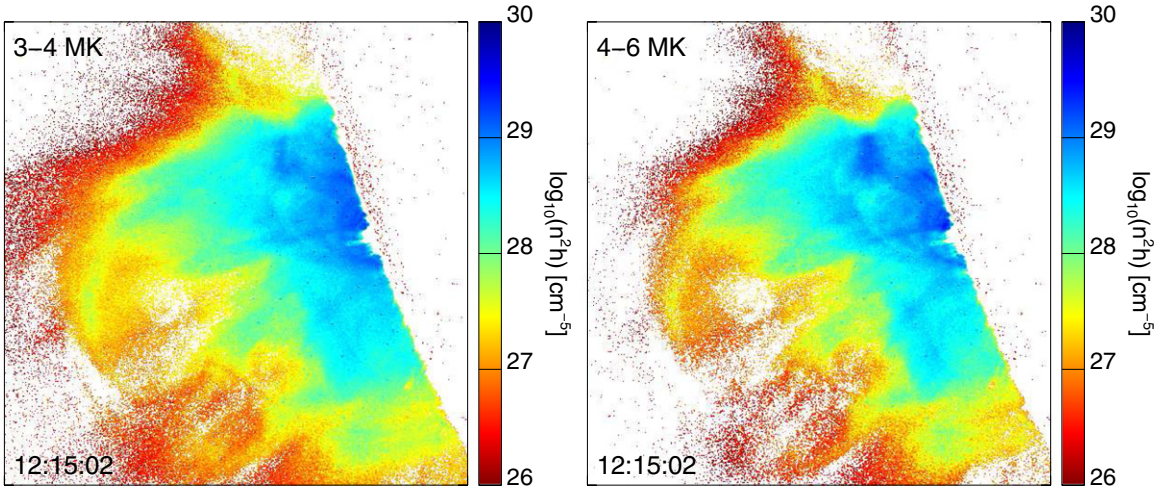


**Figure 5.** Spatial Emission Measure maps at 12:15:02 UT for temperature bins of (left) 3–4 MK and (right) 4–6 MK.
(A color version of this figure is available in the online journal.)

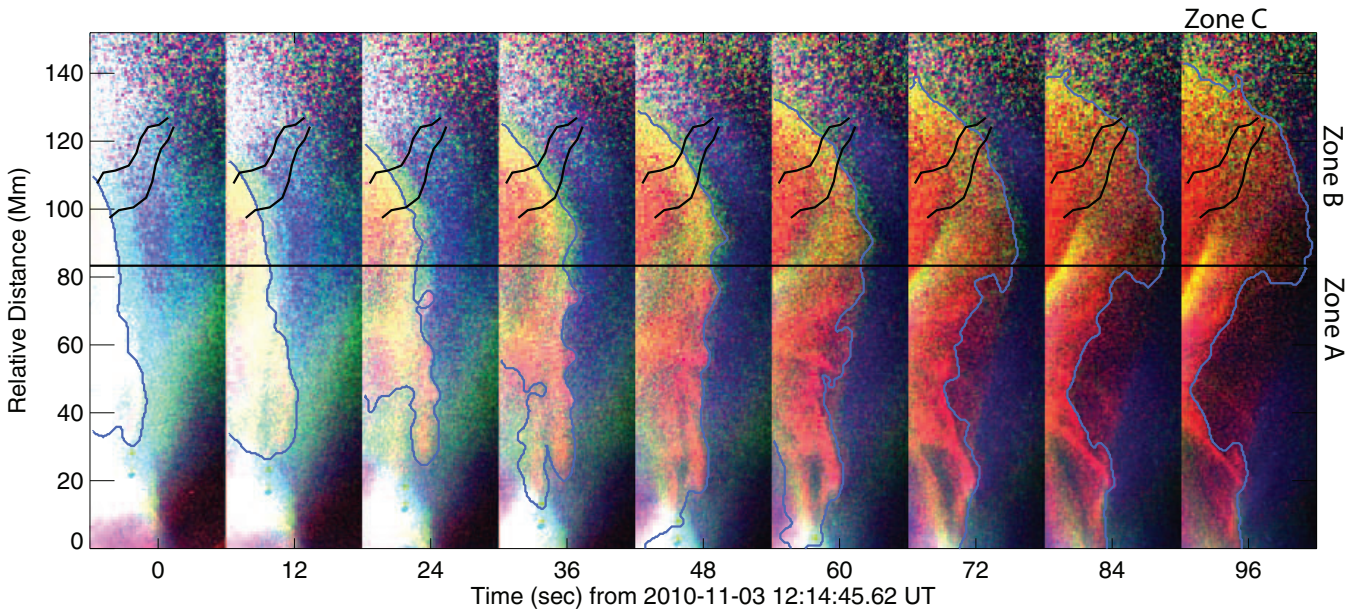


**Figure 6.** Composite time–distance image, showing the development of KH waves on the ejecta northern flank using data from three bandpasses: 131 Å (red), 94 Å (green), and 335 Å (blue). Each image is obtained after average background subtraction and alignment to a common spatial and temporal frame. The temporal frame is the 12 s cadence time frame of the 131 Å data set; the spatial frame is the inertial frame moving with the KH waves observed in 131 Å (the KH structures appear to be standing); the overlaid horizontal and diagonal lines separate three parts or zones: (Zone A) the flank region subject to the KH instability, (Zone B) the flank region ahead of it, and (Zone C) the leading edge.

(A color version of this figure is available in the online journal.)

three bandpasses: 131 Å (red), 94 Å (green), and 335 Å (blue). All snapshots are directed vertically with increasing distance above the solar surface, in the direction of KH wave propagation.

First, the intensity at a given wavelength, $I_\lambda$, is shown relative to an average vertical intensity profile: the average profile is decreasing with height and is obtained by averaging all the snapshot images in the horizontal direction and taking a running smooth average of this profile. Second, the snapshots are aligned in the KH inertial frame: vertical image translations are applied according to the observational "phase speed," $V_k$, connecting related substructures. Finally, all the snapshots are interpolated in the 131 Å time frame to align the plasma structures together: of relevance here, 94 Å, 335 Å, 304 Å, and 211 Å images are taken at the same 12 s cadence but 4.5, 6, −1.5, and 3 s later, respectively, than 131 Å images, so that for a given EUV wavelength we use an average of two adjacent snapshots weighted by appropriate time differences. In order increasing with heights in the vertical direction, we divide the CME flank into three zones: (Zone A) the flank region subject to the KH instability, (Zone B) the flank region ahead of it and (Zone C) the leading edge.

After the initial treatment above, we define regions and their color attributes according to the scheme summarized in Table 1. The proposed scheme draws from a qualitative ordering in the dominating temperature expected for each bandpass: off-limb above active regions or under flaring conditions, the 304, 211, 335, 94, 131 Å bandpasses admit significant response at temperatures of 1.6 MK (Si XI), 2 MK (Fe XIV), 2.8 MK (Fe XVI), 7 MK (Fe XVIII), 11 MK (Fe XXI), respectively (O'Dwyer et al. 2010; see also left panels of Figure 4). It follows that a

**Table 1**
Color Scheme, Definition of Regions Identified from Intensity Differences between EUV Bandpasses and Their Interpretation Inferred from the Ordering of Dominant Bandpass Temperatures and the Mapping Distribution Observed in Figure 8

| Region | Color | Definition | Interpretation |
|---|---|---|---|
| a | Blue | $I_{131} \leqslant I_{335}$ and $I_{94} \leqslant I_{335}$ | Ambient Corona |
| a′ | White | As above, where: ($I_{335} \geqslant I_{304}$ or $I_{335} \geqslant I_{211}$) and ($I_{304} \geqslant 1$ or $I_{211} \geqslant 1$) | Heated or compressed ambient corona (CME-sheath) |
| b | Green | $I_{94} > I_{335} \geqslant I_{131}$ | Heated sheath (viscous layer) |
| c | Yellow | $I_{94} \geqslant I_{131} > I_{335}$ | Boundary layer (primary separatrix bubble) |
| d | Orange | $I_{131} > I_{335}$, $I_{131} > I_{94}$ | Ejecta outer shell (primary reconnection layer) |
| e | Red | $I_{131} > I_{335} \geqslant I_{94}$ and $I_{131} \geqslant 1$ | Ejecta with relatively cooler/hotter material (flux rope) |
| e′ | Black | $1 \geqslant I_{131} > I_{335} \geqslant I_{94}$ | Undefined |

positive deviation in the emission with respect to an average ($I_\lambda \geqslant 1$) indicates larger densities of plasma at this temperature than in the average corona. Furthermore, $I_\lambda$ is intrinsically a proportionality factor between intensity deviation and average, which reflects the proportion of these density deviations ($\propto n_e^2$). Therefore, comparison between two wavelength intensity ratios allows one to qualitatively identify the "dynamically" dominant plasma temperature (with the highest emission variation). First, the primary transition between ejecta and ambient corona is determined by the sign of the difference $I_{131} - I_{335}$, which separates plasma dominated by temperatures at 11 MK if positive and from plasma at 2.8 MK if negative. We then compare the intensity ratios with $I_{94}$ to further separate the regions dominated by temperatures at 7 MK. Figure 7 illustrates the distribution of the data pixels for three horizontal cuts in the snapshot of 12:15:21 UT (fourth snapshot in Figure 6), representative of three identified CME zones, with intensity values plotted in the format $I_{94} - I_{335}$ versus $I_{131} - I_{335}$. Further classifications (primed regions in Table 1) are revealed from ([a′]) additional wavelength ordering using 211 and 304 Å intensities, and ([e′]) no meaningful ordering in the intensity ratios.

The resulting composite color map is shown in Figure 8. It gives a 2D and dynamical view of the plasma regions forming and surrounding the unstable surface. In the right-hand side where we have the ambient corona or sheath regions [a,b], we find regions [a′] (shown in white) that could be more heated or compressed than in the remaining ambient corona [a] (in blue). Both DEM maps and the region maps show that the adjoining region to the ejecta is a CME-sheath, either considerably hotter (green [b] region in Figure 8, 3–4 Mm thick, dominated by temperatures at 7 MK, rather than 11 or 2.8 MK), or slightly hotter (white [a′] region, over 5–10 Mm thick, corresponding to temperatures $T_e = 4.5 \pm 1.5$ MK in Figure 5). For the purpose of defining initial states in the simplest linear MHD description (Equation (1), in the limit of no boundary layer), we will consider the largest region [a′]. These plasma regions are seen in the early stages of the CME and KH development and progressively fade away, starting at a level adjacent to the upper flank region (Zone B) at time 12:15:21 UT (fourth snapshot).

As pointed out in F11 (see also Figures 3 and 6), the left-hand side ejecta region [c,d,e] is formed at least of two sub-regions from observing the emitting ejecta region in 131 Å: the (brighter or red) core and the outer ejecta. Note that this analysis shows a higher degree of structuring than the simplified representation by Cheng et al. (2011), who attribute the overall 131 Å ejecta to a single flux rope cavity region. Thus within the ejecta we identify the flux rope inside a larger outer volume, which we refer to as the outer ejecta shell. In Section 2.2, we did identify this outer ejecta shell with a jet outflow, enclosed beneath a canopy formed by a magnetic field arcade of loops initially connected at both ends to the Sun. On the ejecta side, the most basic plasma conditions for the KH instability onset (density,

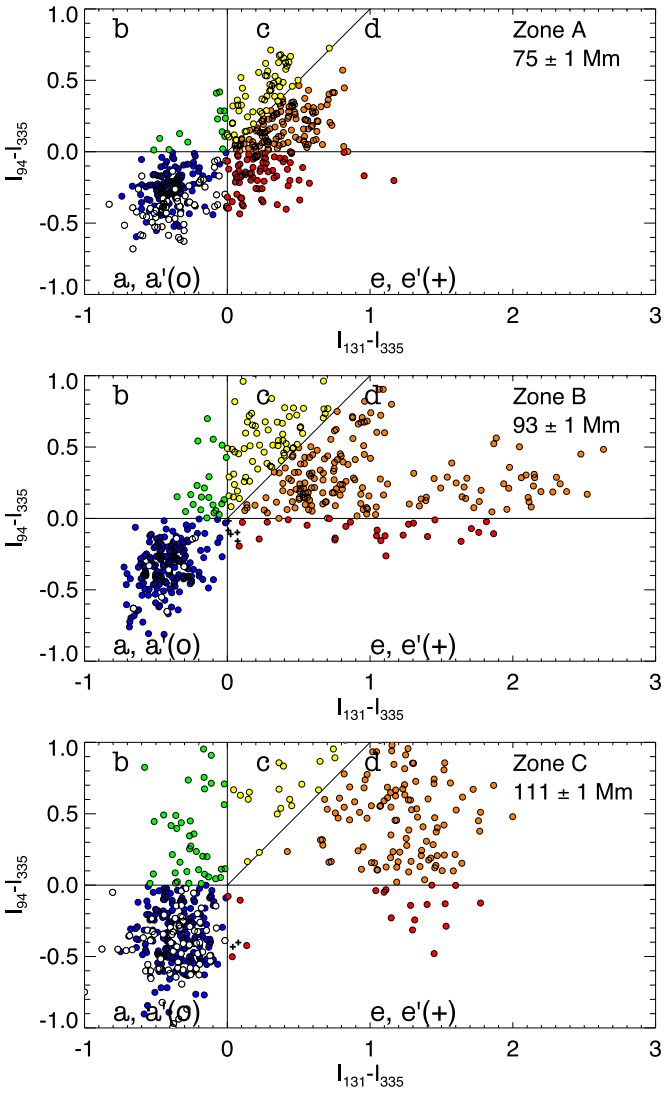


**Figure 7.** Distribution of intensity values, plotted in the format $I_{94} - I_{335}$ vs. $I_{131} - I_{335}$, from a sequence of three horizontal cuts in the snapshot of 12:15:21 UT, representative of three identified CME zones (see Table 1 for labeling).

(A color version of this figure is available in the online journal.)

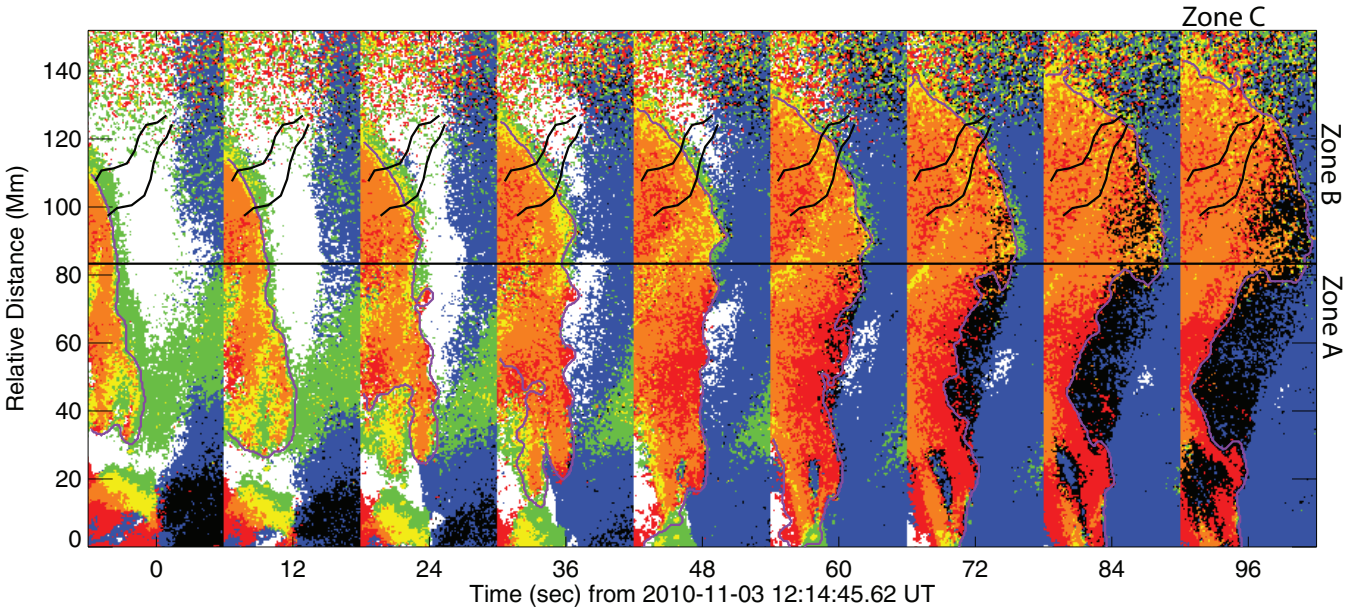


**Figure 8.** Composite time–distance map in the same frame as in Figure 6 giving a 2D and dynamical view of the plasma structuring of the unstable surface. Regions of different colors are identified from intensity differences between EUV bandpasses, as defined in Table 1.

(A color version of this figure is available in the online journal.)

tangential magnetic field, and velocity field in Equation (1)) are prescribed by the conditions in the outer ejecta shell, not by those in the flux rope. The region map of Figure 8 identifies regions [d] (in orange) mostly associated with the outer ejecta shell and regions [e] (in red), that could contain relatively cooler or hotter material than in the main body of the ejecta. At 12:15:21 UT, the ejecta layer in Zone A and studied in Figures 3 and 4 corresponds to regions changing outward from types [d] (in orange) to [e] (in red). This is associated with an outward temperature decrease obtained along the undulating segment (second panel, right column of Figure 4).

Here we note a transition or boundary layer [c] (in yellow), which forms mainly in the upper flank and the leading edge (Zones B and C), but also delineates the lower part of the flux rope. In the upper regions, the plasma conditions in the flux rope and those in the boundary layer progressively mix with those in the outer ejecta shell, rather than replacing them. This can explain the short-duration of the phenomenon: either conditions for the KH instability to occur may be suppressed in this way or the structures overlap in the LOS, making clear identification of KH wave structures difficult. By contrast, we see that the lower ejecta flank regions (Zone A) progressively contain cooler material [e] (red), with intensity variations similar to the ones found in the flux rope, while the adjacent compressed sheath material [a′] (white) appear to decline and other undetermined regions [e′] (black, with no meaningful ordering in the intensity ratios) emerge. Those peculiarities are consistent with the rotation of the overlying ejecta layer (as pointed out in F11) and the formation/lengthening of an underlying reconnecting current sheet (Reeves & Golub 2011; Cheng et al. 2011; Savage et al. 2012). The regions [e] and [e′] found in Zone A could be due to a superposition in the LOS of the ejecta and the compressed sheath material entrained with the rotation.

## 4. IMAGE ANALYSIS

Of particular interest are obtaining an estimate of the velocity shear associated with the KH waves and finding out whether the shear layer thickness compares with the ejecta boundary layer detected through DEM spectral analysis. With remote sensing of the CME, we see the evolution of the outflow jet and its deflections or topological deformations that may result from propagation and expansion against the canopy of overlying field lines. It is reasonable to assume that the AIA 131 Å CME shape is a magnetic field topological surface, in particular at the CME leading edge, where the normal direction to this shape is perpendicular to a magnetic field pile-up. In a frozen-in approximation, this provides some indirect information on the flow field. Thus, by estimating the CME extension in directions normal and parallel to the surface, we attempt to derive effects related to a normal (radial) force and a shearing (meridional) force, respectively.

We extract the CME shapes from the region maps (Figure 9). To a first approximation, the CME flank shape, mostly the upper part, appears parabolic, possibly referring to layered streamlines within the ejecta flow. Note that there is no such parabolic pattern in the CME southern flank, which has an almost opposite oblique shape (Figure 3). At the CME leading edge, the canopy of overlying field lines entrap the outflow layer (Section 2.2), but on the northern flank (Zones B and C), we will assume that the CME flow pattern can be approximated by a parabola or second order polynomial. Parabolas with a vertical axis in the direction of KH propagation are fitted to the B–C portions of each CME shape. In Figure 9, the CME shapes and parabolas are shown in the frame of the KH waves, i.e., Zone A is seemingly at rest. The lower parts of the CME shapes (Zone A) appear to follow the parabolic profiles only in the first two frames. Thus the parabolas are not fitted to Zone A portions of the CME, where the KH waves develop in the early stage (Stage 1, until 12:15:21 UT, time = 36 s) and are fading away in the next (Stage 2). We then derive the radial ($R$) and meridional ($T$) speeds across the series of parabolas (respectively normal and parallel to the parabolic CME surfaces in portions B and C). The velocity vector may be written as $\mathbf{V_k} + \mathbf{U}$ where $\mathbf{U}$ is expressed in curvilinear coordinates ($R$, $T$, $N$),

$$\mathbf{U} = (\mathbf{U_R}, \mathbf{U_T}, \mathbf{U_N}), \quad (4)$$

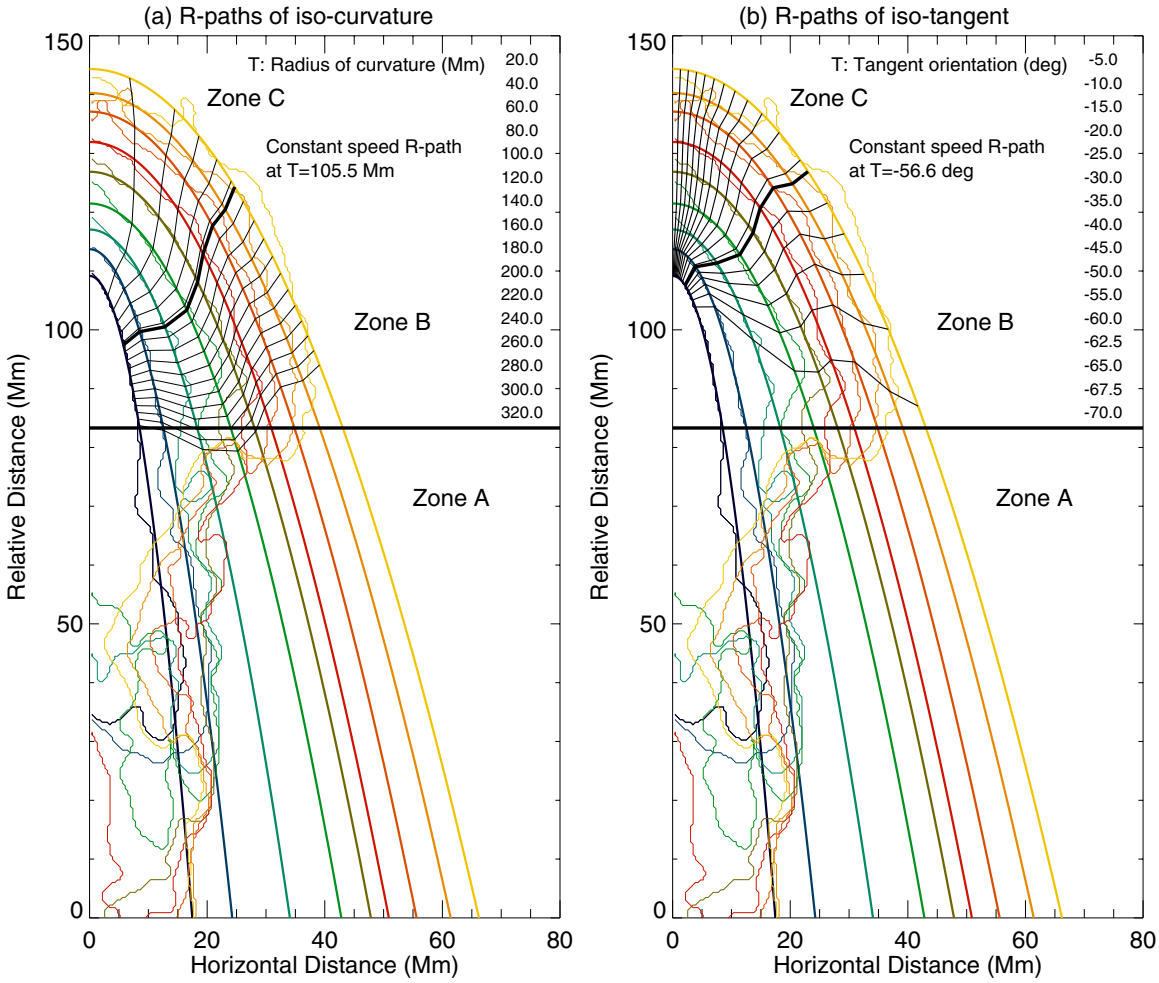


**Figure 9.** Series of CME shapes in the inertial KH-frame, extracted from Figure 8, with parabolas (thick lines) fitted to the Zones B and C portions of each CME shape. The series are shown with colors representing time progression (at 12 s cadence) in order from blue, green, red to yellow shades. Across the series of parabolas are "R-paths" (black lines) connecting points that have either (a) the same radius of curvature or (b) the same tangent orientation, as indicated by meridional $T$-values (covering the Zones B and C). In each geometry, the transition between Zones B and C (diagonal black thick line) corresponds to the R-path with no speed variation between the stages during and after the KH phenomenon.

(A color version of this figure is available in the online journal.)

with the normal direction $N$ in the LOS, and therefore mainly transverse to the propagation axis. We work in one of two different geometrical frames, where the meridional $T$-dimension is either prescribed by the local radius or curvature or by the local tangent orientation. In other words, $T$ is a measure of the position along the CME parabolic profile. We form "R-paths" connecting points across the series of parabolas that have either the same radius of curvature or the same tangent orientation. As illustrated in Figure 9, this leads to distinct R-paths of iso-curvature (panel (a)) and R-paths of iso-tangent (panel (b)), which are traced across the series of parabolas for a range of $T$-values covering the Zones B and C. It may be noted that the two distinct geometrical frames represent limiting cases for tracking planar shapes (same infinite radius of curvature) and circular shapes (same local tangent), respectively. There is an unavoidable ambiguity between parallel and perpendicular motions, associated with tracking time-varying and unknown intermediate shapes. We attempt to resolve this by combining or comparing tracking results from using both limiting cases of geometrical frames. Analysis on the R-paths is conducted systematically in each geometry, as illustrated in Figures 10 and 11, respectively. The upper panels show distances with time along R-paths (left panel (a)) and between adjacent R-paths (right panel (d)). Taking the gradients of these time profiles yields radial and meridional speeds, $U_R$ and $U_T$, as shown in the middle panels for every path in $T$ (i.e., along the CME profile).

In panels (b), both geometrical procedures show that $U_R$ is larger in Zone B during the KH phenomenon (Stage 1) and in Zone C afterward (Stage 2). Those speed measurements express in numbers what could perhaps be observed from closely examining Figure 6 or 7, where, in particular, the expansion perpendicular to the interface can be detected to be stronger first, during Stage 1, in Zone B (thus in the direction perpendicular to the main CME propagation direction), and second, during Stage 2, in Zone C (in the direction of CME motion). The observed KH phase speed is one important characteristic (minimum speed in the direction of CME propagation), which we use as a reference for comparison with the radial expansion speeds (in the KH frame). Panels (b) of Figures 10 and 11 show that, in general, the radial expansion fronts are slower than the KH phase speed ($V_k = 417 \pm 7$ km s$^{-1}$, indicated with a horizontal line), except during Stage 1 (blue dashed curve) in the portion of Zone B closest to Zone A, with the largest radius of

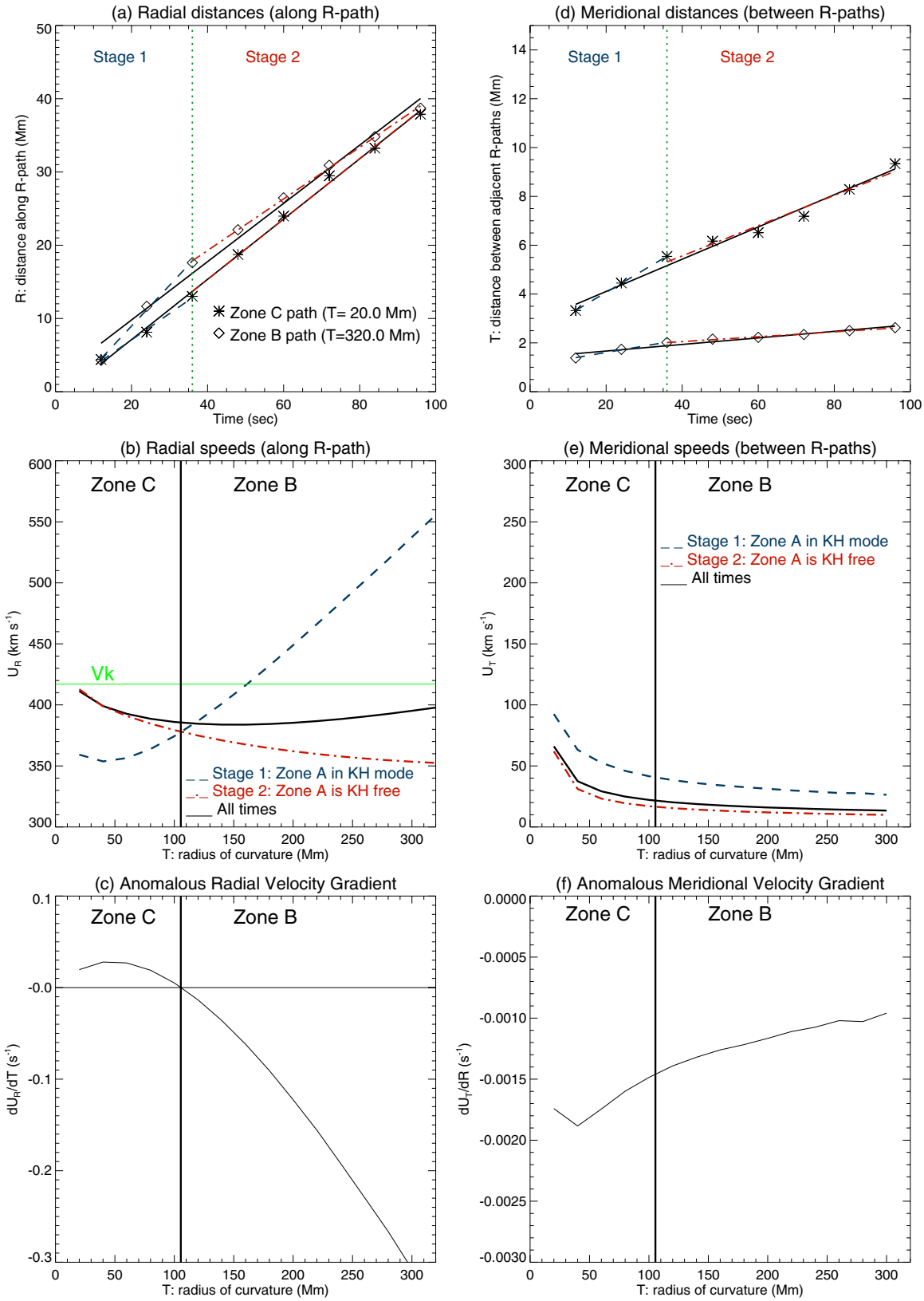


**Figure 10.** Analysis on R-paths of iso-curvature as shown in panel (a) of Figure 9. Upper: distances with time (a) along R-paths and (d) between adjacent R-paths; linear fits in Stage 1 (blue dashed), Stage 2 (red dot-dashed), and at all times (black) are shown for two extreme paths in the $T$-dimension (diamonds and stars); the transition from Stage 1 to Stage 2 is indicated with a vertical (green dotted) line. Middle: linear gradients obtained for every path in $T$, representing (b) radial and (e) meridional speeds, $U_R$ and $U_T$; the KH phase speed, $V_k = 417\,\mathrm{km\,s^{-1}}$, is indicated with a horizontal (green) line. Lower: anomalous gradients (c) in radial velocity, $dU_R/dT$, and (f) in meridional velocity, $dU_T/dR$. The vertical (black) lines at radius of curvature $T = 105.5$ Mm indicates where the radial speed $U_R$ stays constant between Stages 1 and 2.

(A color version of this figure is available in the online journal.)

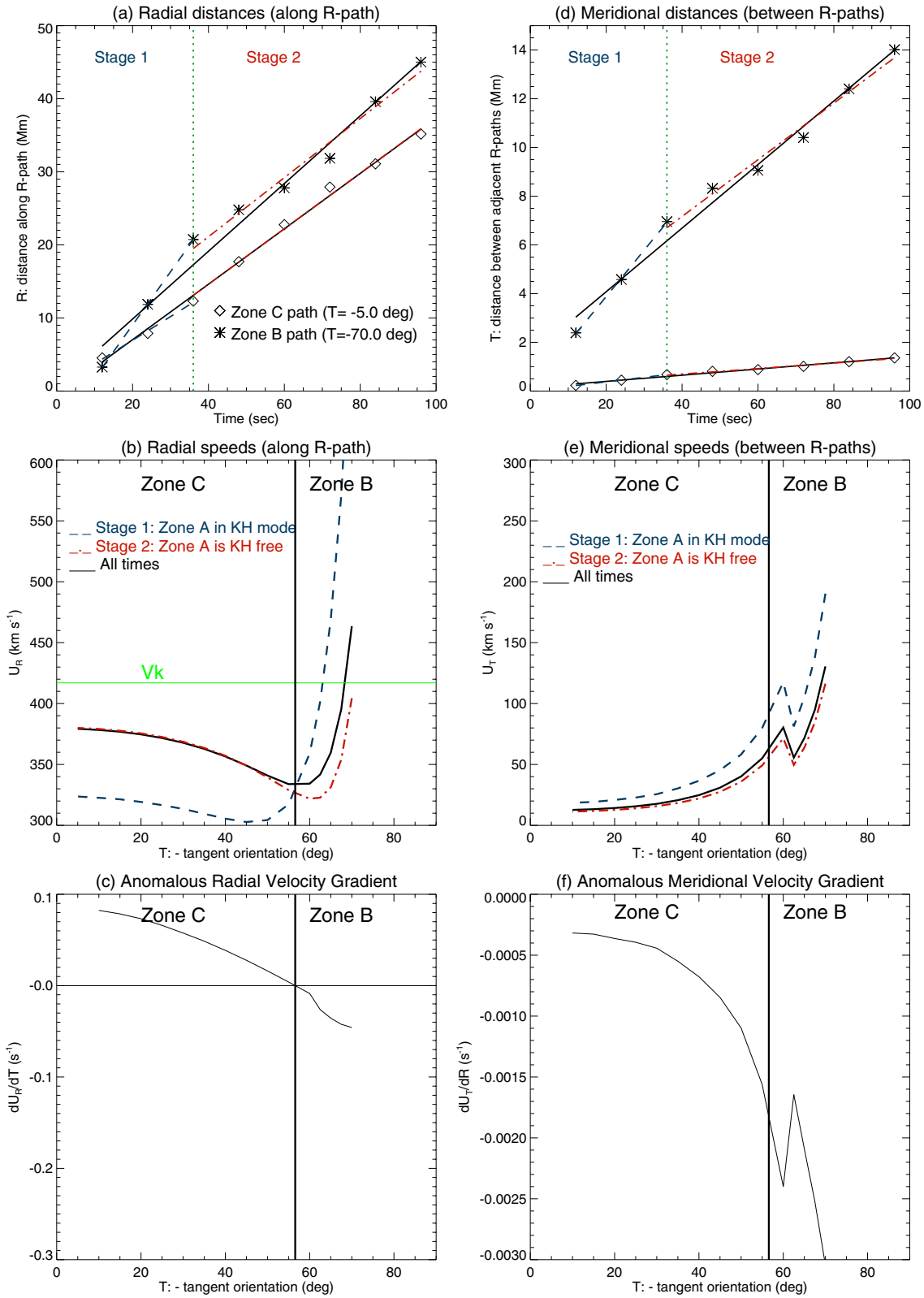


**Figure 11.** Analysis on R-paths of iso-tangent as shown in panel (b) of Figure 9, similar to the one in Figure 10. Constant radial speed $U_R$ between Stages 1 and 2, represented by the vertical (black) lines, occurs at tangent orientation $T = -56.^{\circ}6$.

(A color version of this figure is available in the online journal.)

curvatures or the most vertical tangent orientations. The vertical line indicates the position in $T$ where the radial speed $U_R$ stays constant during and after the KH phenomenon (does not vary between Stages 1 and 2). This occurs at radius of curvature $T = 105.5$ Mm or tangent orientation $T = -56.^{\circ}6$. The corresponding paths are traced in bold in Figures 6, 7, and 9 (diagonal lines). They converge with time and are indicative of the transition between Zones B and C.

We are looking for changes in radial or meridional speeds in the portions B–C of the CME shapes between Stage 2 and Stage 1, that can be attributed to the effects of a finite velocity shear layer associated with the KH waves in Zone A. The so-called anomalous variations are associated here with the non-constant or non-permanent behavior of the KH phenomenon (changes between Stage 1 and Stage 2). We calculate the associated gradient in radial velocity

$$\frac{dU_R}{dT} = \frac{U_{R|_2} - U_{R|_1}}{T_{|_2} - T_{|_1}}, \quad (5)$$

where differences are taken between values from Stages 2 and 1 (the $T$ values in this case are average distances between adjacent R-paths); subscripts beginning with vertical bars are used to indicate Stages or Zones of measurement. As shown in panels (c) of Figures 10 and 11, the gradients obtained in both geometry not only reverse sign in the same fashion at the Zone B and C transition, but are also of the same order (0.1 $s^{-1}$ in absolute value).

In panel (e), both geometrical procedures show that meridional speeds $U_T$ are less than 100 km $s^{-1}$ in Zone C, much lower than the local radial speeds, revealing that radial motion (upward in Zone C) dominates. $U_T$ is also larger during the KH phenomenon (Stage 1) along the whole shape, in both Zones B and C. In panel (f), the corresponding gradient in meridional velocity,

$$\frac{dU_T}{dR} = \frac{U_{T|_2} - U_{T|_1}}{R_{|_2} - R_{|_1}}, \quad (6)$$

is also of the same order ($-0.001$ $s^{-1}$). Variations of the gradient along the CME shape are small: the difference in trend depending on the geometry employed is not significant.

The above measurements show that Zone B expands more radially and meridionally during the KH phenomenon, rather than after; Zone C also expands more meridionally, but does not expand as much radially. This is consistent with the regions [a′] of enhanced pressure in the ambient corona (white in Figure 8), which persist around Zones A and C at the end of Stage 1. In the above analysis, we have neglected the effect of projection, which mainly affects the vertical distances and therefore the speeds in Zone C. However the small projection factor $f = 1.03$ does not affect the magnitude of the rates of shear.

The KH length scales are the wavelength, $\lambda$, and the shear layer, $\Delta L$. The measured wavelength is $18 \pm 0.4$ Mm in the POS (F11), meaning $\lambda = 18.5 \pm 0.5$ Mm in the shear flow direction. There is often a close relationship between gradually varying profiles in velocity field characterizing the shear layer and those in plasma and magnetic field properties characterizing the boundary layer (e.g., Phan et al. 1997; Foullon et al. 2008, in the magnetospheric environment). In this context, we take $\Delta L$ to be the width measurement of $4.1 \pm 0.7$ Mm obtained from the spectral analysis at 12:15:21 UT (Section 3). This value is slightly larger than the theoretical value of $2.33 \pm 0.83$ Mm obtained using results of theoretical investigations showing that $\lambda$ is expected to be 6–12 times $\Delta L$ (Miura 1984). We note a good agreement between the KH wave speed gradient over the ejecta boundary layer detected in Zone A and the detected shear rate in Zone B, *viz*.

$$\frac{V_k}{\Delta L}_{|A} \simeq -\frac{dU_R}{dT}_{|B} \simeq 0.1\ s^{-1}. \quad (7)$$

It is reasonable to assume continuity of the kinetic energy flux between Zones A and B. We thus confirm that the flow vector is more tangential to the CME flank in Zone A than in Zone B and that the shear layer in Zone A is of similar size to the detected boundary layer on the ejecta side.

## 5. RESULTS AND DISCUSSION

### 5.1. Primary Reconnection Outflow Jet as Flow Shear Source

We first consider the cause for the flow shear in the leading ejecta layer as indicated by the presence of the KH phenomenon. In the lower corona imaged by *SDO*/AIA in the 131 Å bandpass, we infer that the ejecta layer corresponds to an "outflow jet," surrounding a hot core or plasmoid on both sides. It is generally believed that the basic energy release mechanism for the outflow jet is magnetic reconnection, but there is still debate on the acceleration mechanism of the jet plasma itself (Shibata et al. 1997; Shimojo & Shibata 2000). The AIA 131 Å ejecta is thus considered to be formed of two parts: (1) the outflow jet layer and (2) the inner plasmoid akin to a flux rope. The outflow jet layer is entrained with the embedded flux rope, that is either pre-existing or formed conjointly in a primary reconnection event, and fills out with hot plasma the space below a canopy of overlying field lines. The primary reconnection event is indicated by the timing $t_0$ (Section 2.2). The asymmetric inflow condition allows net vorticity in the outflow plasmoid (Murphy et al. 2012). Another factor is the asymmetry created by the non-alignment of the outflow jet and flux rope with respect to the canopy axis, which provides a possible return flow on the southern flank. In any case, a flow shear asymmetry between the two flanks is created, which provides a plausible new explanation for the observation of the KH phenomenon on one flank of the ejecta only.

In the classical eruptive flare model with a pre-existing flux rope, a poloidal flux region termed the "separatrix bubble" grows around the original flux rope and similar reconnection layers are expected below the reconnecting current sheet, forming hot flare loops, that are often seen in EUV and X-rays (e.g., Lin et al. 2004, Figure 1). However, one must exert caution in matching the above flare model components to observational counterparts by recalling that the components in this illustration of the eruption are not co-temporal: the current sheet exists prior reconnection, while the separatrix bubble reconnection layers obviously form after reconnection. Thus, it ought to be stressed that, contrary to the interpretation by Cheng et al. (2011, see their Figure 5), the presence of a co-temporal "reconnecting" current sheet below the hot core should be seen as a follow-up process either evolved from or unrelated to the primary reconnecting current sheet responsible for the observed flux rope and reconnection layer, which already form the ejecta. Similarly, in the follow-up process, the observations of post-reconnection upflows and outflows associated with plasmoids or flux tubes (Savage et al. 2012) are regarded as outputs from the "retreating" current sheet layer. It remains to be seen what then can be identified as the separatrix bubble around the original flux rope according to Lin et al. (2004). The identified transition layer [c] surrounding the flux rope (yellow in Figure 8) could be its early manifestation (associated with the primary reconnection event).

The observations in the KH frame show CME curved surfaces (Figure 9), that have radial speeds much larger than meridional speeds (Figures 10 and 11). By contrast, a meaningful flow shear across a one dimensional interface would be required as an initial input parameter for a theoretical 2D description of the KH unstable surface. To adapt the observational results to the 2D theoretical set-up, we can think of the flow shear determined

by the original jet streamline to be more closely prescribed by the parallel streamline to the KH-unstable flank as measured in Zone C, in the direction of KH propagation. The vertical speed in Zone C is $\overline{U_{R|C1}} = 330 \pm 30$ km s$^{-1}$ in Stage 1; the flow shear is thus $V_k + \overline{U_{R|C1}} = 747 \pm 37$ km s$^{-1}$ in the POS, and

$$V_1 = f \times (V_k + \overline{U_{R|C1}}) = 769 \pm 38 \text{ km s}^{-1} \quad (8)$$

along the 3D CME trajectory.

It may be noted that the vertical speed increases to $\overline{U_{R|C2}} = 385 \pm 25$ km s$^{-1}$ in Stage 2, which leads to a total speed $V_k + \overline{U_{R|C2}} = 802 \pm 32$ km s$^{-1}$. Meridional speeds in Zone C are less than 100 km s$^{-1}$ at all stages and would increase the total shear slightly if taken into account. In any case, the latter result is consistent with the speed of the ejecta front tip in the ROI, $833 \pm 5$ km s$^{-1}$ found previously across Stages 1 and 2 from the analysis of the off-limb AIA 131 Å observations (F11), while the true CME leading edge is located outside the ROI and its apparent speed in the direction of CME propagation is found to be lower, at ∼667 km s$^{-1}$ (Bain et al. 2012). The corrected estimated speed at the ejecta nose is $V_{LE} = f \times 667 = 687$ km s$^{-1}$. The result $V_1 > V_{LE}$ showing the flow increasing away from the apex is one seemingly comparable to the magnetosheath flow conditions along the flank magnetopause increasing toward the magnetotail (see F11, Figure 3). However, the flow field obtained indirectly from the observed CME shapes does not give the complete picture of the velocity shear.

### 5.2. CME-sheath from a Piston-driven Shock

Conceptually, for the purpose of our discussion centered on the conditions responsible for the formation of KH waves, we can simplify the geometry to a bipolar environment (Equation (1)), where the CME-sheath is understood as the principal region opposite to the CME-ejecta, in the limit of no boundary layer. The origin of the CME-sheath must be found in the shock forming in the initial stage of the CME formation.

The shock driver is understood here to be the fast acceleration outflow rather than the flux rope. Hence inhomogeneities in speeds across the (non-spherical) surface of the imputed driver, and ensuing asymmetries between CME flanks are likely to generate variations in the shock region at the source of Type-II burst emission. This is supported by several observations. (1) First, Figure 5 show that the CME-sheath layer width on the northern flank gradually decreases at the leading edge, along the curving motion observed earlier in Figure 2, and stops leaving any trace on the southern flank. (2) Second, two curious observations of the Type-II emission from radio imaging observations (12:15:25–12:16:15 UT) were its inward motion and latitudinal (northward then southward) variations as time progressed (Bain et al. 2012): both radio trajectory variations may find some explanation with a draping evolution of the overlying coronal magnetic field at the point perpendicular to the shock that progresses primarily southward and inward with the return outflow; it may also be cautiously speculated that the initial northward latitudinal variation of the radio emission could be associated with the fast lateral ejecta expansion in the northern flank.

The CME-sheath is thus a shocked coronal plasma, and in its more comprehensive geometry, appears as a "cooler envelope" (Bain et al. 2012) with respect to the studied AIA 131 Å ejecta. While the error estimates allow for a density contrast between 0.7 and 1.4, the spectral analysis results imply that the 131 Å KH unstable flank ejecta surface is broadly a surface of discontinuity in temperature and flow, but with possible continuity of density values. One interpretation is that this surface is strongly thermally insulated from the surroundings, due to magnetic and therefore effective thermal connection to the Sun (Chen & Garren 1993), but also due to the closed field topology of the streamer arcade (Pagano et al. 2007). Another explanation is provided by simulations of a temperature pulse akin to a piston or "contact surface" driving a fast MHD shock (Dryer & Maxwell 1979). Processes of adiabatic expansion and compression lead to a maximum density enhancement ahead of the contact surface and a maximum temperature enhancement behind the contact surface. These enhancement values, with respect to local undisturbed values, decline as the CME transient move into the outer corona. In this context, the 131 Å KH unstable ejecta surface would coincide with the region of maximum temperature enhancement.

In its evolved geometry, the CME-sheath can be associated with the wider cavity-part of the CME structure observed later in the white-light coronagraphs. The AIA 131 Å ejecta as observed in the inner corona is likely to form the basis for the bright inner core in the outer corona. Within the classical three-part CME structures (Illing & Hundhausen 1985), differences in accelerations are observed in coronagraph images between the faint features of CME leading edges, imputed to overlying loops, and CME bright knots that presumably entrain flux ropes (Rust et al. 2005). Thus, the coronagraph CME leading edge is considered to form an overlying canopy of field lines ahead of a flux rope (Chen et al. 1997) and may be attributed to fields and mass from the ambient corona either swept up into motion (Illing & Hundhausen 1985) by the rising flux rope and/or brought by magnetic reconnection through the underlying current sheet causing the CME leading edge, akin to a separatrix bubble, to expand (Lin et al. 2004). Further away, as the CME travels in the solar wind, it may be helpful to emphasize how CME/ICME sheaths differ from magnetosheaths, having aspects of both propagation sheaths and expansion sheaths—that is, with reduced lateral deflections away from the nose, and a tendency for the solar wind to pile up, instead of to flow around (Siscoe & Odstrcil 2008).

### 5.3. CME-pause and Linear Instability Conditions

We will next assume that the 131 Å KH unstable interface is a tangential discontinuity, for which the total pressure is conserved. The tangential discontinuity is termed the CME-pause, representing the interface between the shocked "quiet corona" (CME-sheath) and the ejecta. Its 3D-shape was shown, numerically, to be sensitive to the ejecta magnetic field (Evans et al. 2011). As the CME is expanding, pressure balance is established across the flank CME-pause, *viz*.

$$P_1 + \frac{B_1^2}{2\mu_0} = P_2 + \frac{B_2^2}{2\mu_0}, \quad (9)$$

where indices 1 and 2 represent the ejecta and sheath regions, respectively, $P$ is the total thermal pressure, and $P_m = B^2/2\mu_0$ is the magnetic pressure. We disregard the excess of dynamic pressure driving the lateral motion on the ejecta side due to the outflow jet (and anomalous transport contributions due to the KH waves).

The KH length scales are an order $\sim 10^6 \lambda_i$, where the ion inertial length $\lambda_i = c/\omega_{pi} \sim 22.6$ m for $n_e \sim 7.1 \times 10^8$ cm$^{-3}$

**Table 2**
Plasma Parameters across the KH Unstable CME-pause, Observed and Derived with Indicated Main Method or Assumption, Else Inferred from Definition

| Parameter | 1: Ejecta | 2: Sheath | Method/Assumption |
|---|---|---|---|
| $n_e$ | $(7.1 \pm 1.6) \times 10^8$ cm$^{-3}$ | $(7.1 \pm 0.8) \times 10^8$ cm$^{-3}$ | DEM spectral analysis |
| $T_e$ | $11.6 \pm 3.8$ MK | $4.5 \pm 1.5$ MK | DEM spectral analysis |
| $B$ | $7.3 \pm 2.5$ G | 10 G (benchmark) | (1) Pressure balance[a]; (2) PFSS |
| $C_S$ | $557 \pm 94$ km s$^{-1}$ | $347 \pm 60$ km s$^{-1}$ | ... |
| $V_A$ | $635 \pm 277$ km s$^{-1}$ | $806 \pm 30$ km s$^{-1}$ | ... |
| $\beta$ | $1.50 \pm 1.01$ | $0.21 \pm 0.05$ | ... |
| $V$ | $769 \pm 38$ km s$^{-1}$ | $89 \pm 54$ km s$^{-1}$ | (1) Image analysis; (2) Linear theory[b] |
| $\lvert\phi\rvert$ | ... | $90^\circ \pm 44.^\circ7$ | Linear theory[b]($\mathbf{k} \parallel \mathbf{V}$) |
| $M_f$ | $1.01 \pm 0.36$ | $0.10 \pm 0.07$ | ... |

**Notes.**
[a] Pressure balance: under thermal equilibrium.
[b] Linear theory: in the incompressible limit, applied with $n_1 \sim n_2$.

(see also Stasiewicz & Ekeberg 2008). At the KH scales, we can thus work in the quasi-neutrality approximation of MHD, $n_i = n_e$. For a similar hot eruptive event, high ion temperatures of $6.5 \pm 1.5$ MK have been observed at heights of 0.64 $R_\odot$ above the limb, in the Fe XVIII emission line of the *SOHO* Ultraviolet Coronagraph Spectrometer (UVCS), and associated with densities of $2 \times 10^7$ cm$^{-3}$ (Raymond et al. 2003). Since the temperatures and densities in the CME are expected to decrease as the CME propagates at greater height, we can reasonably assume the hot plasma of the ejecta and sheath to be in thermal equilibrium ($T_i = T_e$), and write the expression for the total (electron and ion) thermal pressure as

$$P = n_e k_B T_e + n_i k_B T_i = 2 n_e k_B T_e, \tag{10}$$

where $k_B$ is the Boltzmann constant. The total plasma pressures are $P_1 = 0.245 \pm 0.126$ Pa on the ejecta side and $P_2 = 0.085 \pm 0.019$ Pa on the sheath side.

We choose a benchmark value for the magnetic field $B$ on the sheath side of the CME-pause and determine the magnetic field on the other side from Equation (9). In the quiet corona, the magnetic field reconstruction in Figure 2 shows a loop field line perpendicular, at its apex, to the outflow jet trajectory. At this location, the field strength is $\simeq$10 G. Neglecting variations (decrease with height or increase during the eruption) and taking the sheath field $B_2 = 10$ G as a typical example yields magnetic pressures $P_{m2} = 0.398$ Pa, and thus from Equations (9) and (10), $P_{m1} = 0.238 \pm 0.145$ Pa, and ejecta field $B_1 = 7.3 \pm 2.5$ G. Plasma beta are $\beta_1 = 1.50 \pm 1.01$ and $\beta_2 = 0.21 \pm 0.05$. Observed and derived parameters are summarized in Table 2, including values for Alfvén speeds, $V_A = B/\sqrt{\mu_0 \rho}$, and plasma sound speeds, $C_S = \sqrt{\gamma P/\rho}$, where the ratio of specific heats $\gamma = 5/3$.

We further explore any requirements for the KH instability conditions to be satisfied with the derived input values. One of the arguments in favor of the interpretation in terms of KH waves by F11 was the remarkable proportionality observed between the (projected) propagation velocity of the wave envelope and the ejecta front speed, where the former is half the latter, which may be seen to correspond to limiting cases expected from linear theory (Equation (3) for $V_2 = 0$ and $n_1 = n_2$). Below we further check and quantify how the more detailed observations are consistent with this linear theory. $v_g = f V_k = 429 \pm 8$ km s$^{-1}$ is the meaningful group speed for calculating the wavelength of the KH structure in the direction of propagation. Equation (3) gives an estimate of a flow velocity in the CME-sheath as

$$V_2 = (2 v_g - V_1) + \left(\frac{n_1}{n_2} - 1\right)(v_g - V_1). \tag{11}$$

Given the uncertainties in densities, the magnitude of the second right-hand term arising from a density contrast may be as large as 100 km s$^{-1}$.

In the case of low density contrast ($n_1 \sim n_2$), $V_2 = 2v_g - V_1 = 89 \pm 54$ km s$^{-1}$. This is an acceptable result, since large ($\geqslant$100 km s$^{-1}$) inflows are not detected in this region until after 12:15 UT (in the 131 Å channel, with speeds of 660–690 km s$^{-1}$; Savage et al. 2012). We thus obtain a flow shear

$$V_1 - V_2 = 680 \pm 92 \text{ km s}^{-1} \tag{12}$$

along the CME flank, which is close to the speed of the CME leading edge ($V_{\rm LE} = 687$ km s$^{-1}$). This, also, is consistent with the piston concept (i.e., no evidence of return flow).

We assume **k** aligned with the **V** vectors. This is an educated assumption since the waves are not smeared over in the POS: the substructures appear as coherent, non-dispersive, perturbations (F11), i.e., the KH billows are nicely separated. In other words, if **k** were not approximately in the POS, the wave fronts of the perturbation would overlap, producing a smeared view; this is not observed. Equation (1) simplifies in the form

$$(V_1 - V_2)^2 > 2\left(V_{A,1}^2 \cos^2\phi_1 + V_{A,2}^2 \cos^2\phi_2\right), \tag{13}$$

allowing to estimate the conditions on the required field orientations $\phi = \widehat{(\mathbf{k}, \mathbf{B})}$. For the typical set of plasma parameters ($n$, $B$, and $V$, listed in Table 2), the requirement on the sheath magnetic field tilt angle before KH gets stabilized is (from $\cos^2\phi_1 \geqslant 0$ in Equation (13))

$$|\cos\phi_2| < \frac{|V_1 - V_2|}{\sqrt{2} V_{A,2}}, \tag{14}$$

which indicates a range $|\phi_2| = 90^\circ \pm 44.^\circ7$ of possible tilt angles consistent with wave propagation and flow shear directions most likely quasi-perpendicular to the magnetic field $\mathbf{B_2}$. Conversely, with $|V_1 - V_2| \geqslant \sqrt{2} V_{A,1}$ being met, there is no such restriction on the ejecta magnetic field tilt angle, $\phi_1$.

### 5.4. Reconnection Jet and CME Deceleration

In the context of a reconnection jet (e.g., Shibata et al. 1992; Yokoyama & Shibata 1996), the speed of the outflow is expected to be of the order of the local fast magnetoacoustic speed, $V_f = \sqrt{V_A^2+C_S^2}$ (for shock propagation perpendicular to the magnetic field lines). From the MHD approximation, pressure balance assumption and our choice of parameters above, we infer that $V_{f,1} = 853 \pm 268$ km s$^{-1}$ in the ejecta (see Table 2), which corresponds reasonably well to the speed inferred along the flank ($V_1 = 769 \pm 38$ km s$^{-1}$, see Equation (8)). The fast magnetoacoustic Mach number, $M_f = V/V_f$, is $M_{f,1} = 1.01 \pm 0.36$ on the ejecta side. $M_{f,1}$ provides a characteristic of the developed outflow jet, presumed to be at the origin of the CME. The jet is more or less collimated and the jet surface (northern flank) becomes the KH unstable boundary surface. This result is validated by the following additional considerations.

1. The lowest position of first KH perturbations and upper outflow position in the POS are at heights of about 60 and 120 Mm above the limb, respectively, at time when the first KH perturbations are observed (12:14:51 UT ±6 s, Figure 2 in F11); the jet source site hidden at −14°of longitude behind the limb cannot be lower than 21 Mm below the limb, thus at a position $-10.5 \pm 10.5$ Mm. Taking the projection factor $f$ into account, we deduce the advection length range

$$L_a = [72.6\text{–}134.4] \pm 10.8\,\mathrm{Mm}. \quad (15)$$

   This is well in agreement with the length $V_f \Delta t = 96.8 \pm 36.6$ Mm for advection at outflow speed, $V_f$, since the timing, $t_0$, of the reconnection jet.
2. F11 estimated the exponential growth rate of a structure reaching size of 10 Mm in $30 \pm 6$ s. Using our slightly revised estimate for $\Delta L$ as the initial size, we obtain the revised exponential growth rate

$$\gamma_{\mathrm{KH}} = 0.033 \pm 0.012 \ \mathrm{s}^{-1}. \quad (16)$$

   This revision does not change the consistency of the results with predicted linear growth rates (for compressible plasmas; Miura 1984) that are greater than $0.1 \times (V_1 - V_2)/\Delta L$ for $M_f \geqslant 0.8$.

Rather than an early acceleration phase, this CME event shows a net deceleration in the inner corona. In SECCHI/COR1, the CME appears at 12:45 UT as a partial halo in both *STEREO-B* (SE-SW) and *STEREO Ahead* (*STEREO-A*; E-SSW) located 84° of heliolongitude westward of *SDO*. LASCO coronagraphs show a net deceleration of $-6.94$ ms$^{-2}$, with velocities of less than 300 km s$^{-1}$ appearing at 12:36:06 UT at a distance of 2.79 $R_\odot$ (in C2, see LASCO CDAW CME catalog[6] and Figure 1). The CME leading edge moving into the LASCO/C2 field-of-view is at an apparent height of $1254.55 \pm 10.5$ Mm above the primary reconnection event ($t_0$ = 12:13:00 UT ± 2 s), and is reached with an average transit (apparent) speed of $905 \pm 9$ km s$^{-1}$. This speed may be reconciled with the speed of the AIA CME-sheath of $1296.5 \pm 142.5$ km s$^{-1}$ evaluated during Stage 1 between 12:14 and 12:15 UT (formed using the average of the CME-sheath speeds in 211 Å and 193 Å derived by Bain et al. 2012). The net deceleration in the inner corona is thus $dV_{\mathrm{SH}}/dt = -1.4 \pm 0.2$ km s$^{-2}$ (for a constant acceleration model).

A visual manifestation of the CME drag may be the thin heated sheath (green [b] region in Figure 8) found enveloping the 131 Å ejecta. This layer was found ahead of the KH unstable flank and before the KH waves formed billows, and cannot therefore be interpreted as a direct by-product of the eddy viscosity due to the KH instability. The viscous dissipation time associated with this layer of thickness $\Delta L_{[\mathrm{b}]} = 3.5 \pm 0.5$ Mm, using the traditional kinematic viscosity in the corona ($\nu_{\mathrm{visc}} = 4 \times 10^{13}$ cm$^2$ s$^{-1}$), is

$$\tau_{\mathrm{visc}} \approx \Delta L_{[\mathrm{b}]}^2/\nu_{\mathrm{visc}} = (3125 \pm 875)\,\mathrm{s}, \quad (17)$$

and the corresponding contribution to local deceleration, applied at the leading edge of the CME, can be approximated as

$$\frac{dV_{\mathrm{LE,\,visc}}}{dt} \approx -\nu_{\mathrm{visc}} \frac{V_{\mathrm{LE}}}{(\Delta L_{[\mathrm{b}]})^2} \approx -0.24 \pm 0.07\,\mathrm{km\,s^{-2}} \quad (18)$$

which is an order of magnitude lower and is therefore unlikely to be the main contributor to the deceleration acting on the CME in the first hour or so.

## 6. SUMMARY AND CONCLUSIONS

We have focused our attention on the circumstances and effects associated with the occurrence of the KH phenomenon on the CME northern flank observed in the EUV with *SDO*/AIA. Deriving the CME source surface position in conjunction with *STEREO-B*/EUVI, we have improved the accuracy of all length scales and combinations in the direction of maximum flow shear, originally inferred from POS observations. We have ascertained the timing and early evolution of the CME outflow leading to the instability onset. Performing detailed image and spectral analysis, we have obtained basic plasma parameters and have gained a better understanding of the CME plasma structuring and its parabolic flow pattern. As we evaluated and validated the consistency of the observations with theoretical considerations and predictions, we have answered important questions spurred by this event.

1. We have identified the ejecta layer with a possible reconnection layer surrounding the erupting flux rope. The timing, high temperature (∼11.6 MK), and high flow shear (∼680 km s$^{-1}$) on the northern flank are consistent with the CME reconnection jet origin. This differs from the interpretation in terms of a separatrix bubble as envisaged by Lin et al. (2004).
2. The flow shear on the southern flank is not expected to be as large as on the northern flank, due to the ejecta's jet presumably entrapped by overlying fields and providing a possible return flow. Together with evidence of reconnection on the southern flank, this can explain the observed asymmetry between the CME flanks: parabolic versus oblique shape; KH wave occurrence versus absence of evidence.
3. From the irregular evolution of the CME flow pattern, we have obtained a shear gradient similar to expected spatial flow variations across the layer associated with the KH-unstable flank.
4. The CME is subject to an early deceleration. The outflow layer may act as a temporary piston, generating an initially driven shock ($M_f \simeq 1$). After the pulse acceleration

[6] http://cdaw.gsfc.nasa.gov/CME_list

**Table 3**
CME and KH Wave Parameters in the Shear Flow Direction (Along the 3D CME Trajectory), Obtained from Image Data Analysis, Except in One Instance Where Linear Theory is Applied

| Symbol | Value | Quantity |
|---|---|---|
| $V_{LE}$ | 687 km s$^{-1}$ | Speed of 131 Å CME leading edge |
| $V_1 - V_2$ | $680 \pm 92$ km s$^{-1}$ | Flow shear on the 131 Å CME flank (Linear theory[a]) |
| $v_g$ | $429 \pm 8$ km s$^{-1}$ | KH group speed |
| $\Delta t$ | $111 \pm 8$ s | Lag time of first KH perturbations since onset conditions, $t_0$ |
| $L_a$ | [72.6–134.4] $\pm$ 10.8 Mm | Advection length range |
| $\tau_{KH}$ | $43 \pm 2$ s | KH wave period |
| $\lambda$ | $18.5 \pm 0.5$ Mm | KH wavelength |
| $\Delta L$ | $4.1 \pm 0.7$ Mm | Ejecta boundary layer thickness $\sim$ shear layer thickness |
| $\gamma_{KH}$ | $0.033 \pm 0.012$ s$^{-1}$ | Exponential linear growth rate |

**Note.** [a] Linear theory: in the incompressible limit, applied with $n_1 \sim n_2$.

stops, the (CME-sheath) density disturbances in AIA (corresponding to the white-light CME leading edge) continue to travel and are decelerated (as inferred from the LASCO coronagraphs' observations). Although it was estimated to merely contribute to this deceleration, a possible viscous layer surrounding and interacting with the ejecta was identified.

In the context of recent advances with *SDO* showing evidence for two-stage solar eruptive events on time scales of several hours (Woods et al. 2011; Su et al. 2011), this phase of the linked flare-CME event is associated with the first stage of solar eruption in the low corona (see Woods et al. 2011, their Figure 3 and Table 2). The flare-CME scenario generates two separate sources of particle acceleration, which are spatially and temporally distinct and which also are required to be treated separately energetically. The observed KH phenomenon is here tied to the first source and a low corona ejecta. How the plasma structuring observed in this hot ejecta relates to outer corona and in-situ counterparts is beyond the scope of this paper. Moreover, we have illustrated our discussions with reasonable parameter approximations but with a simplified geometry. The large uncertainty in the results illustrates the limitation of this simple approach and should motivate a more thorough parametric and numerical study. The physical conditions in previous numerical experiments were different than the observed conditions presented here, which can explain why the KH phenomenon in the magnetized corona was not predicted by those experiments before. Observed and derived parameters are summarized in Tables 2 and 3, providing a range of benchmark values from which to build and expand (i.e., exploring the parametric space) in future numerical investigations of the KH waves, intended to develop the seismology of the reconnection layer.

C.F. acknowledges financial support from the UK Science and Technology Facilities Council (STFC) under her Advanced Fellowship ST/I003649/1, a Royal Society International Travel Grant for her visit to LMSAL, USA and a Warwick Research Development Fund award for her visit to ERAU, USA. AIA data is courtesy of *SDO* (NASA) and the AIA consortium. We thank the *SOHO*, *RHESSI*, *STEREO* and *SDO* instrument teams for making available data used in this paper. C.F. and K.N. acknowledge the support by the International Space Science Institute (ISSI, Switzerland) and discussions within the ISSI Team 214 on Flow-Driven Instabilities of the Sun–Earth System. We thank the anonymous referee for useful comments.

*Facilities: SOHO*, *RHESSI*, *STEREO*, *SDO* (AIA)

## REFERENCES

Arge, C. N., Luhmann, J. G., Odstrcil, D., Schrijver, C. J., & Li, Y. 2004, JASTP, 66, 1295
Aschwanden, M. J., & Acton, L. W. 2001, ApJ, 550, 475
Aschwanden, M. J., & Boerner, P. 2011, ApJ, 732, 81
Aschwanden, M. J., Boerner, P., Schrijver, C. J., & Malanushenko, A. 2013, SoPh, 283, 5
Bain, H. M., Krucker, S., Glesener, L., & Lin, R. P. 2012, ApJ, 750, 44
Brueckner, G. E., Howard, R. A., Koomen, M. J., et al. 1995, SoPh, 162, 357
Burlaga, L. F., Sittler, E., Mariani, F., & Schwenn, R. 1981, JGR, 86, 6673
Chandrasekhar, S. 1961, Hydrodynamic and Hydromagnetic Stability (International Series of Monographs on Physics; Oxford: Clarendon)
Chen, J., & Garren, D. A. 1993, GeoRL, 20, 2319
Chen, J., Howard, R. A., Brueckner, G. E., et al. 1997, ApJL, 490, L191
Chen, J., & Kunkel, V. 2010, ApJ, 717, 1105
Cheng, X., Zhang, J., Liu, Y., & Ding, M. D. 2011, ApJL, 732, L25
Das, I., Opher, M., Evans, R., Loesch, C., & Gombosi, T. I. 2011, ApJ, 729, 112
Dryer, M., & Maxwell, A. 1979, ApJ, 231, 945
Evans, R. M., Opher, M., & Gombosi, T. I. 2011, ApJ, 728, 41
Farrugia, C. J., Vasquez, B., Richardson, I. G., et al. 2001, AdSpR, 28, 759
Foullon, C., Farrugia, C. J., Fazakerley, A. N., et al. 2008, JGR, 113, A11203
Foullon, C., Fletcher, L., Hannah, I. G., et al. 2010, ApJ, 719, 151
Foullon, C., Owen, C. J., Dasso, S., et al. 2007, SoPh, 244, 139
Foullon, C., Verwichte, E., Nakariakov, V. M., Nykyri, K., & Farrugia, C. J. 2011, ApJL, 729, L8
Hannah, I. G., & Kontar, E. P. 2012, A&A, 539, A146
Hannah, I. G., & Kontar, E. P. 2013, A&A, in press (arXiv:1212.5529)
Hasegawa, A. 1975, Plasma Instabilities and Nonlinear Effects (New York: Springer)
Howard, R. A., Moses, J. D., Vourlidas, A., et al. 2008, SSRv, 136, 67
Howard, T. 2011, Coronal Mass Ejections: An Introduction (New York: Springer)
Illing, R. M. E., & Hundhausen, A. J. 1985, JGR, 90, 275
Lemen, J. R., Title, A. M., Akin, D. J., et al. 2012, SoPh, 275, 17
Lin, J., Raymond, J. C., & van Ballegooijen, A. A. 2004, ApJ, 602, 422
Liu, Y., Luhmann, J. G., Bale, S. D., & Lin, R. P. 2009, ApJL, 691, L151
Manchester, W. B., IV, Gombosi, T. I., De Zeeuw, D. L., et al. 2005, ApJ, 622, 1225
Miura, A. 1984, JGR, 89, 801
Murphy, N. A., Miralles, M. P., Pope, C. L., et al. 2012, ApJ, 751, 56
O'Dwyer, B., Del Zanna, G., Mason, H. E., Weber, M. A., & Tripathi, D. 2010, A&A, 521, A21
Ofman, L., & Thompson, B. J. 2011, ApJL, 734, L11
Ofman, L., & Thompson, B. J. 2012, ApJL, 760, L19
Pagano, P., Reale, F., Orlando, S., & Peres, G. 2007, A&A, 464, 753
Phan, T. D., Larson, D., McFadden, J., et al. 1997, JGR, 102, 19883
Raymond, J. C., Ciaravella, A., Dobrzycka, D., et al. 2003, ApJ, 597, 1106
Reeves, K. K., & Golub, L. 2011, ApJL, 727, L52
Ruffenach, A., Lavraud, B., Owens, M. J., et al. 2012, JGR, 117, A09101
Rust, D. M., Anderson, B. J., Andrews, M. D., et al. 2005, ApJ, 621, 524
Savage, S. L., Holman, G., Reeves, K. K., et al. 2012, ApJ, 754, 13
Schrijver, C. J., & De Rosa, M. L. 2003, SoPh, 212, 165
Shibata, K., Ishido, Y., Acton, L. W., et al. 1992, PASJ, 44, L173

Shibata, K., Shimojo, M., Yokoyama, T., & Ohyama, M. 1997, in ASP Conf. Ser. 111, Magnetic Reconnection in the Solar Atmosphere, ed. R. D. Bentley & J. T. Mariska (San Francisco, CA: ASP), 29
Shimojo, M., & Shibata, K. 2000, ApJ, 542, 1100
Siscoe, G., & Odstrcil, D. 2008, JGR, 113, A00B07
Stasiewicz, K., & Ekeberg, J. 2008, ApJL, 680, L153
Steinolfson, R. S., & Hundhausen, A. J. 1990, JGR, 95, 15251
Su, Y., Surges, V., van Ballegooijen, A., DeLuca, E., & Golub, L. 2011, ApJ, 734, 53
Talwar, S. P. 1964, JGR, 69, 2707
Terradas, J., Andries, J., Goossens, M., et al. 2008, ApJL, 687, L115
White, R. S., & Verwichte, E. 2012, A&A, 537, A49
White, R. S., Verwichte, E., & Foullon, C. 2012, A&A, 545, A129
Woods, T. N., Hock, R., Eparvier, F., et al. 2011, ApJ, 739, 59
Yokoyama, T., & Shibata, K. 1996, PASJ, 48, 353
Zhang, J., & Dere, K. P. 2006, ApJ, 649, 1100
Zimovets, I., Vilmer, N., Chian, A. C.-L., Sharykin, I., & Struminsky, A. 2012, A&A, 547, A6